frontiers | Frontiers in Electronic Materials

TYPE Review
PUBLISHED 21 June 2023
DOI 10.3389/femat.2023.1174159



OPEN ACCESS

EDITED BY
Jie Su,
Xidian University, China

REVIEWED BY
Chong Chen,
Chinese Academy of Sciences (CAS), China
Zhuo Xu,
Shaanxi Normal University, China

*CORRESPONDENCE
Harshit Sharma,
harshit.npl19a@acsir.res.in

RECEIVED 28 February 2023
ACCEPTED 19 May 2023
PUBLISHED 21 June 2023

CITATION
Sharma H and Srivastava R (2023), Solution-processed pristine metal oxides as electron-transporting materials for perovskite solar cells.
*Front. Electron. Mater.* 3:1174159.
doi: 10.3389/femat.2023.1174159



# Solution-processed pristine metal oxides as electron-transporting materials for perovskite solar cells

Harshit Sharma[1,2]* and Ritu Srivastava[1,2]

[1]CSIR-National Physical Laboratory, New Delhi, India, [2]Academy Of Scientific and Innovative Research (AcSIR), Ghaziabad, India

In recent years, perovskite material-based photovoltaic devices have attracted great attention of researchers because of an expeditious improvement in their efficiency from 3.8% to over 25%. The electron transport layer (ETL), which functions for the extraction and transportation of photogenerated electrons from active perovskite material to the electrodes, is a vital part of these perovskite solar cells (PSCs). The optoelectronic properties of these electron transport layer materials also have an impact on the performance of these perovskite solar cells, and for commercialized flexible perovskite solar cells, low-temperature and solution-processable electron transport layers having high stability and suitable optoelectronic properties are needed. In this regard, the solution-processable films of different metal oxides have been largely investigated by many research groups. So, this review summarizes the optoelectronic properties of the different metal oxide-based electron transport layers and the development in the performance of the perovskite solar cells, which have solution-processable metal oxides as electron transport layers.

KEYWORDS

**electron transport layers, metal oxides, perovskite solar cell, sol–gel process, hybrid perovskite materials**

## 1 Introduction

Solar energy, a green energy source, is the demand of the time as conventional energy sources cannot deal with the present and future energy crises in the world. For harvesting solar energy, bulk silicon wafer-based solar cells (SCs), which are the first-generation SCs, have successfully been developed and commercialized (Liu et al., 2018). However, they have limited power conversion efficiency (PCE), and the cost of these is also high as the material is used in bulk (Andreani et al., 2019). To address the high cost of solar cells, there has been research into the second-generation solar cell technologies, such as thin-film silicon solar cells and thin-film heterojunction-based solar cells (Shah et al., 1995). However, the PCE of these SCs also remains limited. So, a solar cell that has high stability, high PCE, and low cost needs to be developed and commercialized. In this respect, third-generation solar cells like organic solar cells (OSCs), perovskite solar cells (PSCs), and quantum dot solar cells (SCs) are of great interest in research because of their potential for high PCE (Brown and Wu, 2009; Tvrdy and Kamat, 2011; Khatibi et al., 2019). In these, the PSCs have attracted the eye of the researchers more because of a significant increase in the PCE from 3.8% to 25.5% (as certified by the Best Cell-Efficiency Chart in 2022 shown in Figure 1) (Best Cell-Efficiency Chart NREL, 2021). PSCs have a basic construction in which an active perovskite layer is placed between a hole-transporting layer (HTL) and an electron-transporting layer (ETL) (Hussain et al., 2018). The active layer is used to absorb the light and create the hole–electron pairs (i.e., the excitons) in the devices. Although the carrier (i.e., electron or hole) transport layers (CTLs) are used

for the efficient extraction and transportation of these carriers from the active layer to the electrodes. The performance of PSCs depends upon the stability of active material and the stability of these CTLs, i.e., these CTLs also play a vital role in achieving high stability and the high PCE of SCs (Wang et al., 2019a). For a high PCE, these CTLs should have many optical and electrical properties like high electron/hole mobility, high blocking ability to the counter carriers, a wide band gap, and high transparency to ensure the light passes through them with minimal absorbance (Ansari et al., 2018). These CTLs should also show a high compatibility and ohmic contact with the adjacent active layer and the electrode. In addition to these, for the better extraction of the electrons, the conduction band (C.B.) of the ETL should match the lower unoccupied molecular orbit (LUMO) of the active layer and for the better extraction of holes; the valence band (V.B.) of the HTL should match the higher occupied molecular orbit (HOMO) of the active layer (Ren et al., 2019). As the cost of solar is also a major factor for its commercialization, the CTLs should be processable via solution process methods that are cost-effective and highly compatible with large-scale printing of flexible solar cells. Metal oxides like $TiO_2$, ZnO, $SnO_2$, $Nb_2O_5$, $CeO_x$, $WO_3$, and $In_2O_3$ for ETLs are the ideal materials that meet such requirements (Kojima et al., 2009; Kumar et al., 2013; Song et al., 2015; Singh et al., 2016; Wang et al., 2019b). These metal oxides show high stability in the ambient environment, and these can be processable via solution process methods, which make these useful for large-scale and flexible solar cell devices. For the ETL, $TiO_2$ has been investigated a lot as it has a wide band gap and high transparency. However, it also has low carrier mobility and also needs a high temperature (~500 °C) for better crystallinity, leading to better performance of SCs. So, the materials like $SnO_2$ and ZnO are emerging as an alternative to $TiO_2$ because these can be processed at a relatively low temperature, and these materials possess a wider band gap, higher electron mobility, and higher transparency. In addition to these binary metal oxides, other inorganic materials like $BaSnO_3$, $SrTiO_3$, $SrSnO_3$, $ZrSnO_4$, and $(CH_3)_2Sn(COOH)_2$ have also been developed and investigated as an ETL for futuristic PSCs (Bera et al., 2014; Shin et al., 2017; Guo et al., 2019a; Li et al., 2020; Noh et al., 2020). The aim of this review is to present a comprehensive analysis of binary metal oxide-based solution-processable ETLs used in PSCs.

## 2 Perovskite solar cells

In PSCs, perovskite materials (having a general chemical formula $ABX_3$, where A and B are cations and X is an anion) such as $CH_3NH_3PbI_3$, $CH_3NH_3PbCl_3$ $CH_3NH_3PbBr_3$, and $CsPbBr_3$ are used as an absorber layer for harvesting the light (Mesquita et al., 2017). This is why the term "perovskite solar cell" is being used for this type of solar cell. The crystal structure of these perovskite materials is shown in Figure 2.

The organic-metal halide perovskites consist of an organic cation [i.e., $CH_3NH_3^+$ (methyl-ammonium), $CH_3CH_2NH_3^+$ (ethyl-ammonium), and $NH_2CH = NH_2^+$ (formamidinium)], a divalent metal cation (i.e., $Pb^{2+}$, $Sn^{2+}$, and $Ge^{2+}$), and a monovalent halogen anion (i.e., F-, Cl-, Br-, and I) (Ono et al., 2017). For photovoltaic

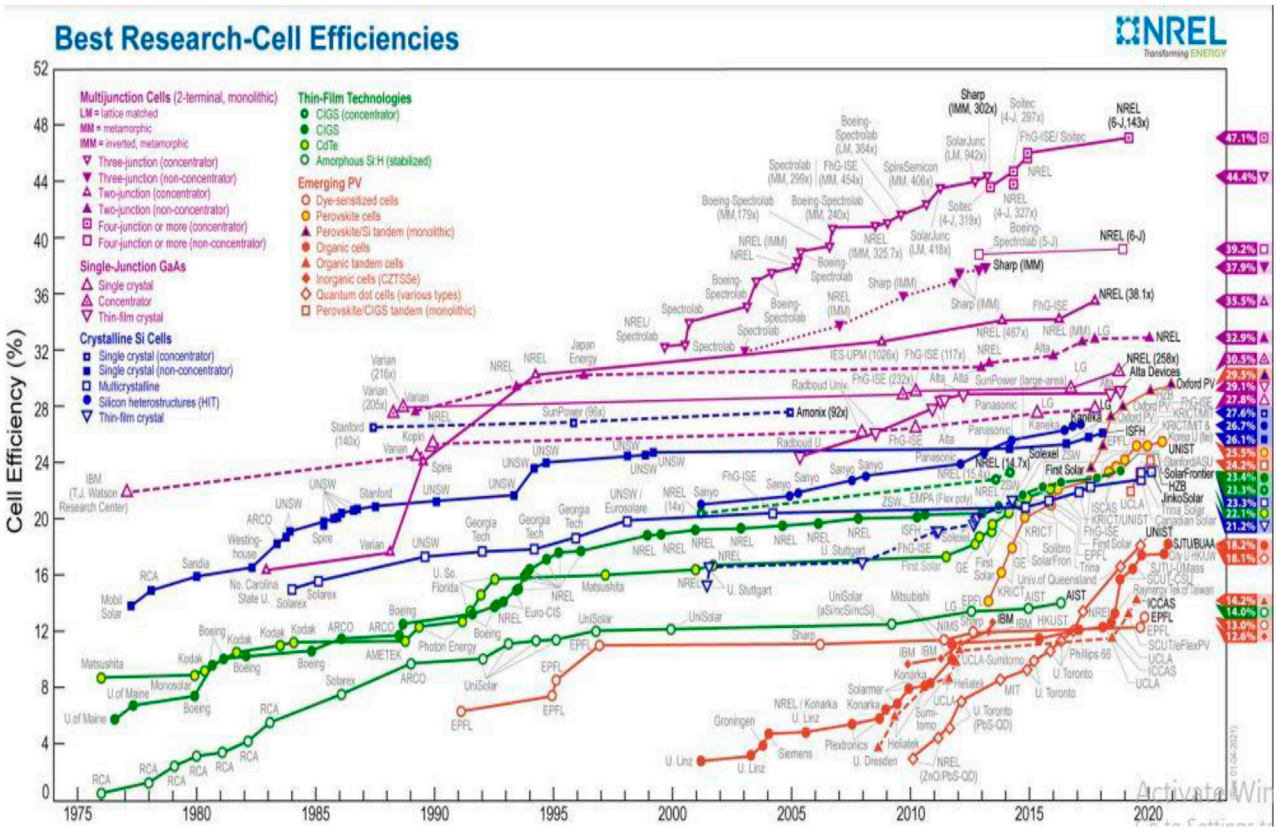


FIGURE 1
Achieved efficiencies of different SCs. Adapted from the National Renewable Energy Laboratory (Best Cell-Efficiency Chart NREL, 2021).

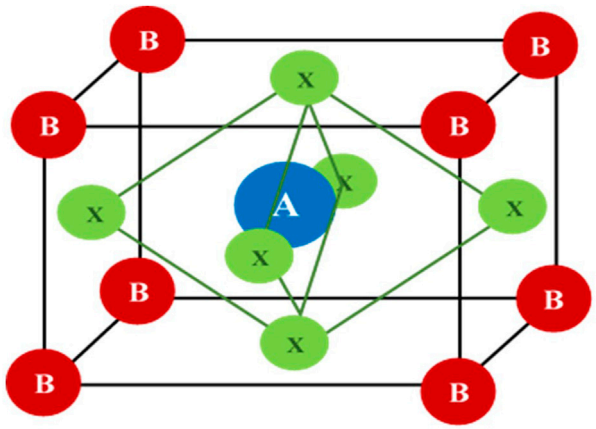


FIGURE 2
Crystal structure of a perovskite material.

applications, perovskite materials have first been investigated by Kojima et al. (2009) who fabricated the two different PSCs with $CH_3NH_3PbBr_3$ and $CH_3NH_3PbI_3$ as absorbing layers, having PCE of 3.1% and 3.81%, respectively. After this, $CH_3NH_3PbI_3$ (methylammonium lead iodide or $MAPbI_3$) has largely been investigated in PSCs because it has a small band gap (1.5–1.6 eV) and a wide absorption spectrum up to 800 nm.

## 2.1 Structure

The perovskite solar cell has a general structure, in which the active perovskite material film is sandwiched between the ETL and HTL, and the transparent conducting oxide (TCO) contact layer with a backing of the glass substrate and metal contacts have been attached with the corresponding ETL and HTL based on the structure. If the TCO layer exists adjacent to the ETL, the configuration is known as the n–i–p configuration, or if the TCO exists adjacent to the HTL, it is known as the p–i–n configuration or the inverted structure. The PSCs have been further divided into a planar and mesoporous structure. In the planar structure, only the compact layer of the transporting material is used. If the configuration is n-i-p, then it is a planar heterojunction PSC; otherwise, it is an inverted planar heterojunction solar cell, as shown in Figures 3A,B respectively. However, in the mesoporous (n-i-p) structure, the mesoporous scaffold layer either of n-type material or the inert $Al_2O_3$ is added, as shown in Figure 3C, and in the mesoporous (p-i-n) structure, the mesoporous scaffold layer either of p-type material or the inert $Al_2O_3$ is added, as shown in Figure 3D. These scaffold layers help in the formation of the pin-hole-free film of perovskite material and also in better extraction of the carriers.

## 2.2 Working mechanism

When the light falls on a PSC and enters into the perovskite layer either passing through the ETL or HTL, the perovskite material absorbs the light and creates the pairs of electron–hole carriers, i.e., excitons, as shown in Figures 4A,B. Then, these carriers get diffused into the absorber layer and collected via ETL and HTL materials, respectively, at the boundaries and have been transported to the respective electrodes, and the external circuit connected to it gets the power (Jung and Park, 2015). For the efficient collection of carriers, the diffusion length of excitons should be high, and also, the thickness of the absorber layer should be less than the diffusion length of excitons so that the high number of carriers can be collected by transporting materials before their recombination happens.

# 3 Metal oxides for ETLs

For collecting the carriers from the absorber and transporting them to the corresponding electrodes, the ETL plays a crucial role. Therefore, for a better outcome of the solar cell, these ETLs should also possess some important properties like high carrier mobility, large-band gap, better energy level alignment with the absorber

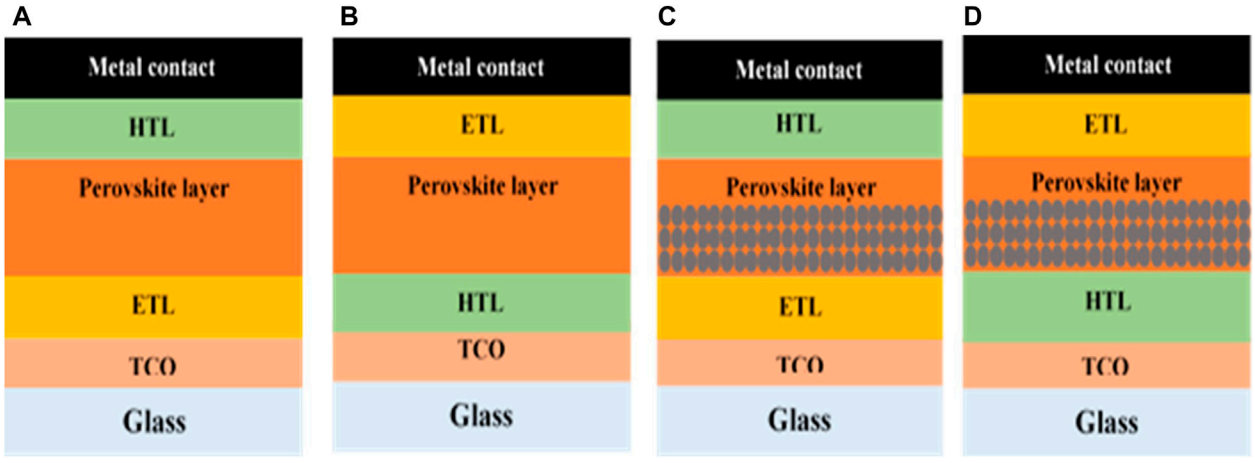


FIGURE 3
Different configuration of PSCs: **(A)** planar (n-i-p) heterojunction structure, **(B)** inverted planar (p-i-n) heterojunction structure, **(C)** mesoporous (n-i-p) heterojunction structure, and **(D)** mesoporous (p-i-n) heterojunction structure.

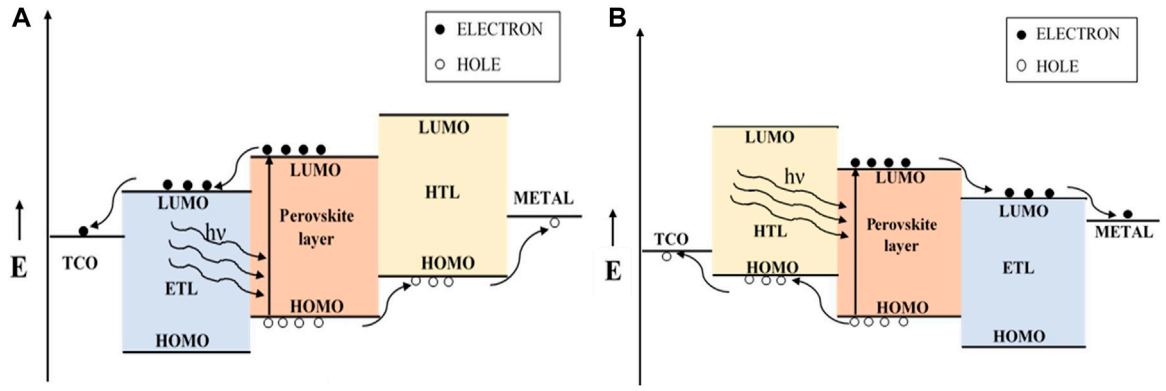


FIGURE 4
Band diagram of PSCs in **(A)** regular structure and **(B)** inverted structure.

layer, high transparency to the light, high conductivity, high stability, and better adhesivity to the absorber layer. In addition to these, for the low cost and flexible device, these can also be processable via vacuum-free and low-temperature solution process techniques. The metal oxides like $TiO_2$, ZnO, $SnO_2$, $CeO_x$, $WO_x$, $InO_x$, and $NbO_x$, have optoelectronic properties suitable for ETLs, and these can also be processed via solution-processable methods like spin coating, chemical bath deposition, electro-spray, spray pyrolysis, and screen-printing methods. Some advantages and disadvantages of these metal oxides as an ETL have been

**TABLE 1 Advantages and disadvantages of different metal oxides as ETLs.**

| Material | Advantage | Disadvantage | Reference |
|---|---|---|---|
| **$TiO_2$** | High optical transparency | Low electron mobility | Jung and Park (2015) |
| | High band gap | Needs high annealing temperature | Seo et al. (2005) |
| | | | Green et al. (2014) |
| **ZnO** | High electron mobility | Presence of the -OH group on the surface leads to perovskite degradation | Sun et al. (2011) |
| | Wider band gap | | Yang et al. (2015) |
| **$SnO_2$** | High electron mobility | Low crystallinity at low-temperature growth and the presence of cracks in high-temperature growth | Wang et al. (2020a) |
| | Wider band gap | | Zhu et al. (2019) |
| | High transparency | | |
| | Deeper conduction band minimum | | |
| | Low-temperature annealing for growth | | |
| | Small hysteresis | | |
| **$WO_x$** | Stable in harsh and corrosive environments, high electron mobility (10–20 $cm^2$/V-sec) | Corresponding PSCs are more sensitive to the ambient atmosphere | Gheno et al. (2017) |
| **$NbO_x$** | Wide optical band gap (~4.1-eV) | Low electron mobility | Zhou et al. (2020) |
| | High transmission | | |
| | Suitable conduction band energy level | | |
| **$In_2O_3$** | Wide band gap (~3.75 eV) | Poor surface coverage of the film | Lau et al. (2015); Korotcenkov et al. (2005) |
| | Low-temperature-processable | | |
| | High electron mobility (~20 $cm^2$/V-sec) | | |
| **$CeO_x$** | Wide band gap | Low electron mobility (~0.01 $cm^2$/V-sec) | Suzuki et al. (2004), Orel and Orel (1994), GarcÃa-SÃ¡nchez et al. (2010) |
| | High ionic conductivity | | Zhou et al. (2020) |
| | High thermal and chemical stability | | |

summarized in Table 1. Furthermore, the development in PCE and the other properties of the PSCs based on these solution-processable metal oxide ETLs have been discussed.

## 3.1 Titanium dioxide ($TiO_2$)

As an ETL material in PSCs, $TiO_2$ is a promising material as its optical and electrical properties favor electron extraction. In PSCs, $TiO_2$ has been investigated in the form of a compact layer (c-$TiO_2$) and a mesoscopic layer (m-$TiO_2$). $TiO_2$ has the properties like a wider band gap (~3.1 eV), the electron mobility of the order of 1 $cm^2$/V-sec, a conduction band minimum (CBM, i.e., LUMO level) of ~ −4.1 eV, and a valence band maximum (VBM, i.e., HOMO level) of ~ −7.2 eV with reference to the vacuum level (Seo et al., 2005; Green et al., 2014; Jung and Park, 2015). These properties favor the efficient extraction of electrons from the active material. The favorable conduction band minimum alignment of the $TiO_2$ helps in the efficient extraction of the electrons, and the deeper valance band maximum blocks the movement of the holes from the perovskite layer to $TiO_2$. Because of these, $TiO_2$ has been used widely as an ETL material. In addition to these favorable properties, $TiO_2$ has some drawbacks too like the low electron mobility and the need for a high temperature for the crystalline film. For the better electrical conductivity of $TiO_2$, the nano-crystalline film is required and for this, there is a need

**TABLE 2 Performance of $TiO_2$-based PSCs.**

| Deposition technique | Precursor | Device structure | Annealing temperature | $V_{oc}$ (V) | $J_{sc}$ (mA/$cm^2$) | F.F. | PCE (%) | Year | Reference |
|---|---|---|---|---|---|---|---|---|---|
| Spin coating + Doctor blade method | Titanium diisopropoxide bis(acetylacetonate) and $TiO_2$ paste | FTO/$TiO_2$/m-$TiO_2$/$MAPbI_3$/spiro-OMeTAD/Au | 550 °C | 0.88 | 17.0 | 0.62 | 9.7 | 2012 | Kim et al. (2012) |
| Spray pyrolysis | Titanium diisopropoxide bis(acetylacetonate) | FTO/$TiO_2$/m-$Al_2O_3$/$MAPbI_2Cl$/spiro-OMeTAD/Ag | 550 °C | 0.98 | 17.8 | 0.63 | 10.9 | 2012 | Lee et al. (2012) |
| Spin coating + hydro thermal | Titanium (IV) n-butoxide | FTO/$TiO_2$/$TiO_2$ nanorods/$MAPbI_3$/spiro-OMeTAD/Au | 550 °C | 0.95 | 15.6 | 0.63 | 9.4 | 2013 | Kim et al. (2013a) |
| Spin coating + hydro thermal | Tetrabutyl titanate | FTO/$TiO_2$/$TiO_2$ nanowire array/$CH_3NH_3PbI_2Br$/spiro-OMeTAD/Au | 550 °C | 0.82 | 10.12 | 0.59 | 4.87 | 2013 | Qiu et al. (2013) |
| Spin coating | Titanium isopropoxide | FTO/$TiO_2$/$MAPbI_{3-x}Cl_x$/spiro-OMeTAD/Ag | 500 °C | 1.07 | 21.5 | 0.67 | 15.4 | 2013 | Liu et al. (2013) |
| Spin coating | Titanium isopropoxide | FTO/$TiO_2$/m-$Al_2O_3$/$CH_3NH_3PbI_{3-x}Cl_x$/spiro-OMeTAD/Ag | 500 °C | 1.02 | 17.8 | 0.66 | 11.8 | 2013 | Docampo et al. (2013) |
| Spin coating | Titanium isopropoxide | FTO/PEDOT:PSS/$CH_3NH_3PbI_{3-x}Cl_x$/$PC_{60}BM$/$TiO_x$/Al | 130 °C | 0.94 | 15.8 | 0.66 | 9.8 | 2013 | Docampo et al. (2013) |
| Spin coating | Titanium isopropoxide | PET/ITO/PEDOT: PSS/$CH_3NH_3PbI_{3-x}Cl_x$/$PC_{60}BM$/$TiO_x$/Al | 130 °C | 0.88 | 14.4 | 0.51 | 6.4 | 2013 | Docampo et al. (2013) |
| Spin coating + Doctor blade | Ti(IV) bis (ethyl acetoacetate) diisopropoxide | FTO/c-$TiO_2$/m-$TiO_2$/$MAPbI_3$/spiro-OMeTAD/Au | 450 °C | 0.90 | 18.1 | 0.48 | 7.8 | 2013 | Kim et al. (2013b) |
| Spray pyrolysis and screen printing | Titanium diisopropoxide bis(acetylacetonate) and $TiO_2$ paste | FTO/c-$TiO_2$/m-$TiO_2$/$MAPbI_3$/spiro-OMeTAD/Au | 550 °C | 0.63 | 14.5 | 0.53 | 4.85 | 2014 | Ito et al. (2014) |
| Spin coating | $TiO_2$ nanoparticles and titanium di isopropoxide bis(acetylacetonate) | FTO/$TiO_2$/m-$Al_2O_3$/$MAPbI_{3-x}Cl_x$/spiro-OMeTAD/Ag | 150 °C | 1.05 | 20.0 | 0.72 | 15.3 | 2014 | Wojciechowski et al. (2014) |
| Spin coating | $TiCl_4$ | FTO/$TiO_2$/m-$TiO_2$/$MAPbI_3$/spiro-OMeTAD/Au | 450 °C | 1.05 | 19.8 | 0.64 | 13.7 | 2014 | Yella et al. (2014) |
| Spin coating | $TiO_2$ nanoparticle dispersion | ITO/$TiO_2$/$CH_3NH_3PbI_{3-x}Cl_x$/P3HT/Ag | 135 °C | 0.93 | 21.0 | 0.69 | 13.6 | 2014 | Conings et al. (2014) |
| Spin coating | Titanium diisopropoxide bis(acetylacetonate) and $TiO_2$ paste | FTO/$TiO_2$/m-$TiO_2$/$MAPbI_3$/spiro-OMeTAD/Au | 500 °C | 1.07 | 17.4 | 0.74 | 13.9 | 2014 | Kim and Park (2014) |

(Continued on following page)

**TABLE 2 (*Continued*) Performance of $TiO_2$-based PSCs.**

| Deposition technique | Precursor | Device structure | Annealing temperature | $V_{oc}$ (V) | $J_{sc}$ (mA/cm$^2$) | F.F. | PCE (%) | Year | Reference |
|---|---|---|---|---|---|---|---|---|---|
| Spray pyrolysis | Titanium bis(acetyl acetonate) and $TiO_2$ paste | FTO/$TiO_2$/m-$TiO_2$/$MAPbI_3$/spiro-OMeTAD/Au | 500 °C | 0.87 | 17.37 | 0.58 | 8.76 | 2014 | Wu et al. (2014) |
| Spray pyrolysis and Spin coating | Titanium bis(acetyl acetonate) and $TiO_2$ paste | FTO/$TiO_2$/m-$TiO_2$/$MAPbI_3$/CuSCN/Au | 500 °C | 19.7 | 1.01 | 0.62 | 12.4 | 2014 | Qin et al. (2014) |
| Spray pyrolysis and screen printing | Diisopropoxide titanium bis(acetylacetonate) and $TiO_2$ nanosheets | FTO/$TiO_2$/$TiO_2$ nanosheets/m-$ZrO_2$/$MAPbI_3$/carbon | 500 °C | 0.86 | 20.1 | 0.61 | 10.64 | 2014 | Rong et al. (2014) |
| Spin coating | Titanium di isopropoxide bis(acetylacetonate) and $TiO_2$ paste | FTO/$TiO_2$/m-$TiO_2$/$MAPbI_3$/spiro-OMeTAD/Au | 500 °C | 1.05 | 21.64 | 0.74 | 17.01 | 2014 | Im et al. (2014) |
| Spin coating | Titanium di isopropoxide bis(acetylacetonate) and $TiO_2$ paste | FTO/$TiO_2$/m-$TiO_2$/$MAPbI_3$/spiro-OMeTAD/Au | 550 °C | 1.02 | 20.02 | 0.76 | 14.46 | 2014 | Lee et al. (2014) |
| Spray coating | $TiO_2$ nanoparticles in isopropanol | FTO/$TiO_2$/$MAPbI_3$/spiro-OMeTAD/Ag | - | 0.92 | 22.76 | 0.67 | 14.30 | 2017 | Huang et al. (2017a) |
| Chemical bath deposition | $TiCl_4$ | FTO/$TiO_2$/$MAPbI_3$/spiro-OMeTAD/Au | 100 °C | 1.01 | 20.06 | 0.63 | 12.62 | 2017 | Liang et al. (2017) |
| Spin coating | Titanium di isopropoxide bis(acetylacetonate) and $TiO_2$ paste | FTO/$TiO_2$/m-$TiO_2$/$MAPbI_3$/spiro-OMeTAD/Au | 500 °C | 1.06 | 22.03 | 0.75 | 17.51 | 2017 | Jeong et al. (2017) |
| Chemical bath deposition | $TiCl_4$ | FTO/nanoflower $TiO_2$/$MAPbI_3$/spiro-OMeTAD/Ag | 500 °C | 1.09 | 24.3 | 0.72 | 19.1 | 2020 | Lu et al. (2020) |
| Spin coating | $TiCl_4$ | PEN/ITO/$TiO_2$/$MAPbI_3$/spiro-OMeTAD/Au | 150 °C | 1.11 | 22.32 | 0.656 | 16.11 | 2021 | Yang et al. (2021a) |
| Spin coating + hydrothermal method | Titanium diisopropoxide bis(acetylacetonate) + $TiO_2$ nanorods/nanoparticles | FTO/$TiO_2$/$TiO_2$ nanorods + nanoparticles/$MAPbI_3$/CuSCN/Au | 500 °C | 1.048 | 22.50 | 0.59 | 14.14 | 2021 | Nguyen et al. (2022) |
| Spin coating | $TiCl_4$ | FTO/$TiO_2$/m-$TiO_2$/$(FAPbI_3)_{0.85}$ $(MAPbBr_3)_{0.15}$/Spiro-OMeTAD/Au | 500 °C | 1.10 | 23.72 | 0.64 | 16.81 | 2022 | Han et al. (2022) |
| Bar coating | Titanium di isopropoxide bis(acetyl acetonate) | FTO/$TiO_2$/m-$TiO_2$/$MAPbI_3$/spiro-OMeTAD/Au | 500 °C | 0.9 | 23.3 | 0.57 | 12.1 | 2022 | Mandati et al. (2022) |
| Aerosol spray pyrolysis | Titanium di isopropoxide bis-(acetylacetonate) | FTO/$TiO_2$/$Cs_{0.05}(FA_{0.85}MA_{0.15})_{0.95}Pb(I_{0.85}Br_{0.15})_3$/PCBM/Au | 450 °C | 1.08 | 23.12 | 0.76 | 19.21 | 2022 | Culu et al. (2022) |
| Spin coating | Titanium butoxide | FTO/$TiO_2$/Hc-$TiO_2$/$MAPbI_3$/spiro-OMeTAD/$MoO_3$/Ag | 500 °C | 1.15 | 20.70 | 0.77 | 20.85 | 2023 | Bao et al. (2023) |

for high-temperature (~500 °C) annealing (Green et al., 2014). This requirement of high-temperature annealing limits the use of $TiO_2$ for flexible photovoltaic devices. The performance of some $TiO_2$ ETL based PSCs have been summarized in Table 2.

In 2009, when Kojima et al. (2009) introduced the first perovskite-based photovoltaic device, $TiO_2$ had been used as the ETL material. In this work, the $TiO_2$ film was fabricated by using the $TiO_2$ paste post-treated at 480 °C temperature for 1 h. The $TiO_2$/$MAPbI_3$ heterojunction-based cell gave the best PCE of 3.81%. In the solution-processed methods, the most common precursor for the fabrication of the compact $TiO_2$ film is titanium diisopropoxide bis(acetylacetonate). In 2012, Kim et al. (2012) first introduced the all-solid-state PSCs having the structure of FTO/$TiO_2$/m-$TiO_2$/$MAPbI_3$/spiro-OMeTAD/Au, where the spiro-OMeTAD has been used as the HTL. In these PSCs, the c-$TiO_2$ has been fabricated by the spin coating method with titanium diisopropoxide bis(acetylacetonate) as a precursor, while the m-$TiO_2$ was fabricated by the doctor blade coating methods using the

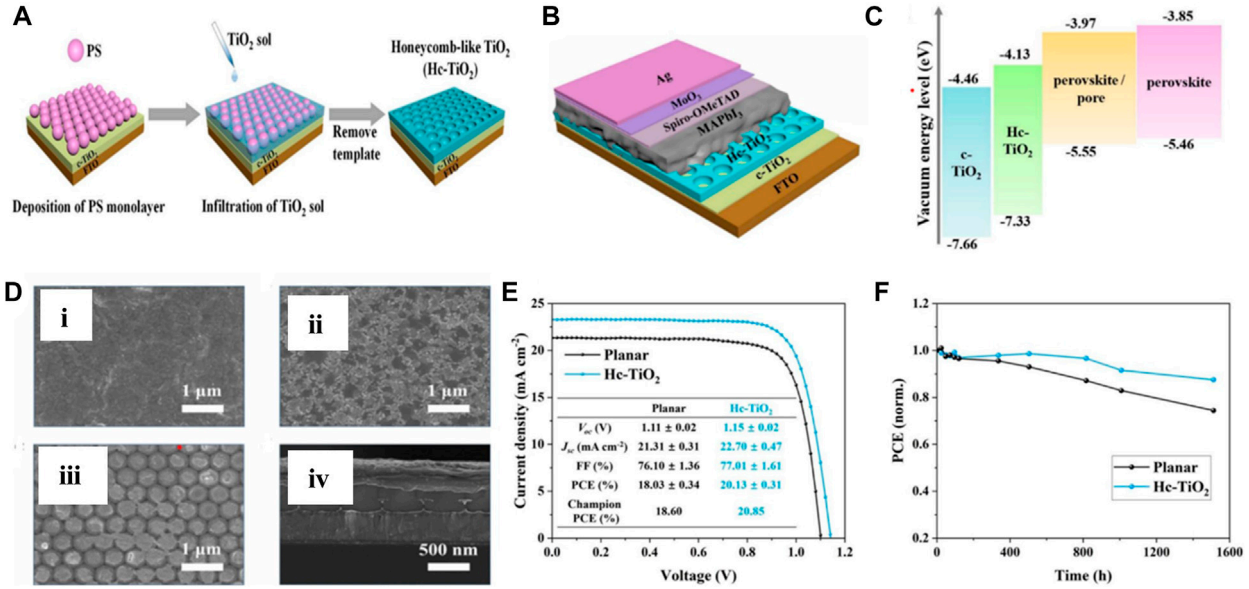


FIGURE 5
**(A)** Schematic representation of Hc-$TiO_2$ deposition, **(B)** structure of FTO/$TiO_2$/Hc-$TiO_2$/$MAPbI_3$/spiro-OMeTAD/$MoO_3$/Ag PSCs, **(C)** band structure of corresponding PSCs, **(D)** SEM image of perovskite/c-$TiO_2$ (i), perovskite/Hc-$TiO_2$(ii), perovskite/pore (iii), and cross-sectional structure of corresponding PSCs, **(E)** J-V curve and parameter, and **(F)** stability of corresponding PSCs. Reproduced with permission from Bao et al. (2023).

nanocrystalline $TiO_2$ paste. These PSCs resulted in a champion PCE of 9.7%. Lee et al. (2012) had fabricated mesoporous PSCs of the structure of FTO/$TiO_2$/m-$Al_2O_3$/$MAPbI_2Cl$/spiro-OMeTAD/Ag, which resulted in a champion efficiency of 10.9%. In these PSCs, the c-$TiO_2$ layer was deposited by the spray pyrolysis method. Kim et al. (2013a) used the nanorods of the rutile-phase $TiO_2$ prepared via a hydrothermal method to form the m-$TiO_2$ layer in PSCs, and the corresponding PSCs resulted in the champion PCE of 9.4% for 0.6-μm length of nanorods, and it decreased as the length of the nanorods increased. Liu et al. (2013) used the spin-coated $TiO_2$ films on the FTO substrate to fabricate the planar PSCs having $MAPbI_{3-x}Cl_x$ as an active material, which was deposited using the vapor deposition method, and these simple planar structured cells gave the best PCE of 15.4% without any complex structure. Docampo et al. (2013) had investigated the $TiO_x$ film prepared via spin coating and a low temperature (~130 °C) post-annealing in the inverted structure PSCs. These inverted configuration cells delivered the best PCE of 9.8% and 6.4% on FTO-coated glass substrates and an ITO-coated flexible substrates, respectively. In addition to the spin coating and the spray pyrolysis method, the $TiO_2$ ETLs have also been fabricated the via chemical bath deposition (CBD) method (Liu et al., 2013; Liang et al., 2017). Liang et al. (2017) fabricated the low-temperature (100 °C) annealed $TiO_2$ film via the CBD method using $TiCl_4$ as a precursor for the PSCs having the structure of FTO/$TiO_2$/$MAPbI_3$/spiro-OMeTAD/Au. The device resulted in a PCE of 11.18%, and the treatment of $TiO_2$ films with UV-ozone improved the PCE to 12.62%. Lu et al. (2020) had also opted for the same CBD method and the same device structure, but they had delicately treated the $TiCl_4$ precursor via KOH, which changes the morphology of the film, and hence, the device performance with a champion PCE of 19.1% have been achieved.

Yang et al. (2021a) had opted for a low-temperature (~150 °C) annealing process for anatase $TiO_2$ film growth for fabricating flexible PSCs with the PEN/ITO/$TiO_2$/$MAPbI_3$/spiro-OMeTAD/Au structure. For the deposition of the $TiO_2$ film, they synthesized the colloidal $TiO_2$ solution via the sol–gel method, which was used as a precursor for the $TiO_2$ layer. The concentration of the precursor has been optimized to 2 mol/L for full coverage and aggregation-free films, which resulted in 16.11% efficiency. Recently, Bao et al. (2023) had investigated a honeycomb (Hc) type $TiO_2$ film as an ETL in PSCs with FTO/$TiO_2$/Hc-$TiO_2$/$MAPbI_3$/spiro-OMeTAD/$MoO_3$/Ag structure, as shown in Figure 5. To fabricate the interconnecting Hc-$TiO_2$ network, the sacrificial template method has been opted. This Hc-$TiO_2$ network has a periodicity of around 450 nm, resulting in an additional light trapping at this wavelength scale. Hc-$TiO_2$ showed a better band alignment with perovskite than the compact $TiO_2$, and the perovskite crystal film has a preferred orientation along the (110) plane due to the confinement in the Hc-$TiO_2$ pores, which reduced the trap density. The corresponding PSCs have yielded a PCE of 20.85% and showed a high tolerance toward the change in the optical path with changing the incident angle of the light.

## 3.2 Zinc oxide (ZnO)

$TiO_2$ needs a high annealing temperature for suitable morphological, electrical, and optical properties to show high performance of the PSCs, which limits its use for a flexible photovoltaic device. So, an alternative that exhibits the same or better characteristics with low temperature treatment is needed to develop for highly efficient new-generation flexible photovoltaic devices. In this regard, ZnO is the first material as an alternative to

**TABLE 3 Performance of ZnO-based PSCs.**

| Deposition technique | Precursor | Device structure | Annealing temperature | $V_{oc}$ (V) | $J_{sc}$ (mA/cm$^2$) | F.F. | PCE (%) | Year | Reference |
|---|---|---|---|---|---|---|---|---|---|
| Electro-deposition + CBD | $Zn(NO_3)_2{\cdot}6H_2O$ | FTO/ZnO/ZnO nanorod $MAPbI_3$/spiro-OMeTAD/Au | 90 °C | 1.02 | 16.98 | 0.51 | 8.90 | 2013 | Kumar et al. (2013) |
| Spin coating | ZnO nanorod colloidal solution | FTO/ZnO/$MAPbI_3$/spiro-OMeTAD/Ag | 400 °C | 0.68 | 12.7 | 0.58 | 5.2 | 2013 | Bi et al. (2013) |
| Spin coating | ZnO nanoparticle solution | ITO/ZnO/$MAPbI_3$/spiro-OMeTAD/Ag | R.T. | 1.03 | 20.4 | 0.75 | 15.7 | 2014 | Liu and Kelly (2014) |
| Spin coating | $Zn(CH_3COO)_2{\cdot}2H_2O$ and ZnO nanorod solution | FTO/ZnO/ZnO nanorod $MAPbI_3$/spiro-OMeTAD/Au | 450 °C | 0.99 | 20.08 | 0.56 | 11.13 | 2014 | Son et al. (2014) |
| Spin coating | $Zn(CH_3COO)_2 2H_2O$+ ethanolamine in 2-methoxyethanol | ITO/ZnO/$MAPbI_3$/PTB7-Th/$MoO_3$/Ag | 290 °C | 0.86 | 14.31 | 0.68 | 8.37 | 2014 | Kim et al. (2014) |
| Spin coating + electrospray | $Zn(CH_3COO)_2{\cdot}2H_2O$ | FTO/ZnO/m-ZnO $MAPbI_3$/spiro-OMeTAD/Ag | 350 °C | 1.01 | 16.0 | 0.67 | 10.8 | 2014 | Mahmood et al. (2014a) |
| Spin coating + hydrothermal method | $Zn(CH_3COO)_2{\cdot}2H_2O$ | FTO/ZnO/ZnO nanorod/$MAPbI_3$/spiro-OMeTAD/Ag | 350 °C | 0.92 | 18.0 | 0.62 | 10.35 | 2014 | Mahmood et al. (2014b) |
| Spin coating | ZnO nanoparticle solution | ITO/ZnO/MAPbI3/P3HT/Ag | R.T. | 0.98 | 17.4 | 0.67 | 11.4 | 2015 | Yang et al. (2015) |
| Spray | ZnO nanoparticle solution | FTO/ZnO/$MAPbI_3$/CuI/Au | 150 °C | 0.55 | 14.21 | 0.44 | 3.47 | 2016 | Zhu et al. (2016) |
| Spin coating | $Zn(CH_3COO)_2{\cdot}2H_2O$+ ethanolamine in 2-methoxyethanol | ITO/ZnO/MAPbI3/P3HT/Ag | 140 °C | 0.93 | 14.99 | 0.62 | 8.77 | 2017 | Mahmud et al. (2017) |
| Spin coating | $Zn(CH_3COO)_2{\cdot}2H_2O$ | ITO/ZnO/$CsPbBr_2I$/Spiro-OMeTAD/Ag | 150 °C | 1.04 | 8.78 | 0.52 | 4.8 | 2018 | Aamir et al. (2018) |
| Spin coating | Anhydrous zinc acetate + poly-ethylene glycol | ITO/ZnO/$MAPbI_3$/spiro-OMeTAD/Ag | 125 °C | 1.01 | 19.2 | 0.59 | 11.5 | 2020 | Liu et al. (2020) |
| Spin coating | $Zn(CH_3COO)_2{\cdot}2H_2O$+ methanol amine in 2-methoxyethanol | FTO/ZnO/$MAPbI_3$/spiro-OMeTAD/Ag | 140 °C | 0.75 | 19.9 | 0.68 | 10.39 | 2020 | Ahmadi et al. (2020) |
| Slot die coating | $Zn(CH_3COO)_2{\cdot}2H_2O$+ ethanolamine in 2-methoxyethanol | FTO/ZnO/$Cs_{0.17}FA_{0.83}Pb(I_{0.83}Br_{0.17})_3$/Spiro-OMeTAD/carbon | 180 °C | 0.96 | 15.53 | 0.73 | 10.81 | 2021 | Khambunkoed et al. (2021) |
| Spin coating | ZnO nanoparticles | FTO/ZnO/$(FAPbI_3)_{0.9}(CsPbBr_3)_{0.1}$/Spiro-OMeTAD/Ag | 120 °C | 1.16 | 22.88 | 0.79 | 21.15 | 2021 | Leng et al. (2021) |
| Spin coating | ZnO QDs | FTO/ZnO/triple cation perovskite/PTAA/Au | 150 °C | 1.129 | 22.93 | 0.77 | 20.05 | 2022 | Chavan et al. (2022) |
| Spin coating + hydrothermal | ZnO QDs and $Zn(NO_3)_2.6H_2O$ | FTO/ZnO QDs/ZnO NRs/$MAPbI_3$/PTAA/Ag | 350 °C | 1.01 | 19.14 | 0.64 | 10.69 | 2022 | Jarwal et al. (2022) |

$TiO_2$, which has been investigated by the researchers. It has a large band gap of ~3.4 eV, higher electron mobility (200–205 $cm^2V^{-1}$ $s^{-1}$), and the HOMO and LUMO energy levels are also similar to $TiO_2$ (Sun et al., 2011). In addition to these, it can crystallize at a lower temperature, which makes it a potential alternative to $TiO_2$ for flexible PSC devices. ZnO-based PSCs have some drawbacks as well like the presence of hydroxyl (−OH) radicals at the ZnO film surface, which reacts with perovskite materials and leads to its degradation (Yang et al., 2015). It limits the performance and stability of the corresponding PSCs. Still, many research groups have investigated it as an ETL in PSCs and also tried to tackle these challenges. The performance of some ZnO ETL based PSCs have been summarized in Table 3. Kumar et al. (2013) had investigated the low-temperature (˂100 °C) processed ZnO film for the PSC application. For preparing the compact film of ZnO, the electro-deposition technique was opted and a film of the nanorod ZnO was fabricated over the compact layer by the CBD method; corresponding PSCs resulted in the best PCE of 8.9% on a rigid substrate, while only 2.62% on a flexible substrate. Liu and Kelly (2014) had used the ZnO nanoparticle dispersion solution in a mixture of butanol, chloroform, and methanol solvents in a 70:5:5 ratio as a precursor for spin coating

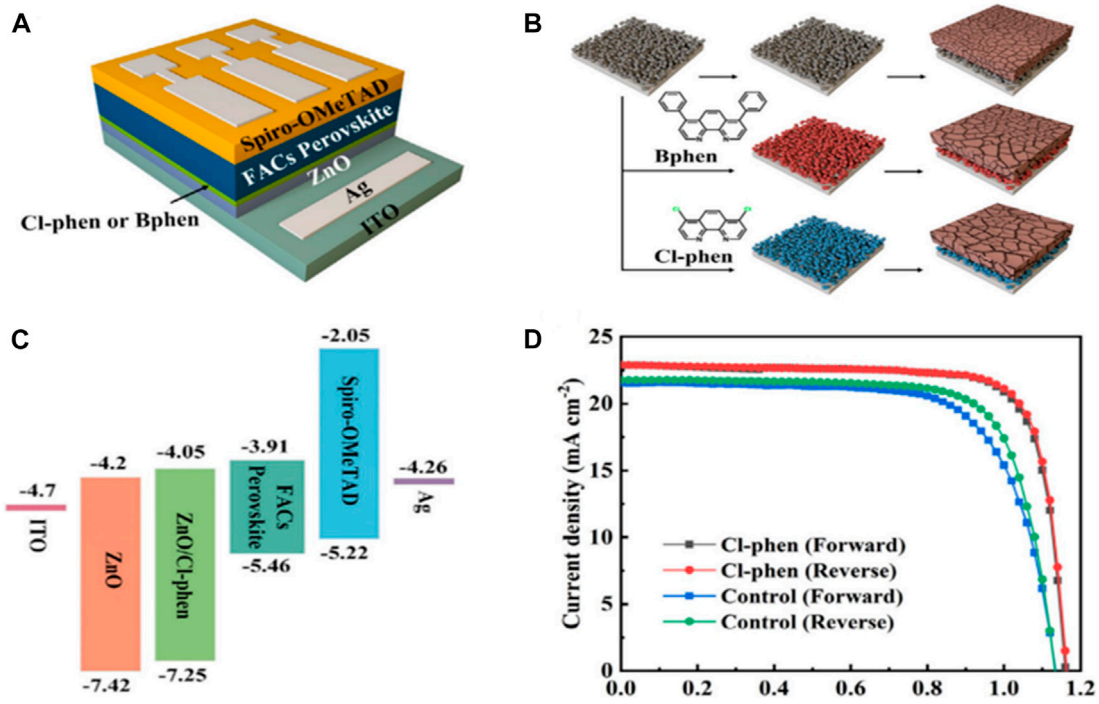


FIGURE 6
**(A)** Device structure of the phenanthroline derivatives/ZnO bilayer-based PSC. **(B)** Schematic representation of additive treatment and its effect on the perovskite grain size. **(C)** Energy-level diagram of the materials layer. **(D)** J-V curve of corresponding PSCs. Reproduced with permission from Leng et al. (2021).

the ZnO ETL to fabricate the cell of ITO/ZnO/$MAPbI_3$/spiro-OMeTAD/Ag structures and achieved a 15.7% efficiency. Ahmadi et al. (2020) had investigated the suitable solvent to prepare the precursor solution for the deposition of ZnO ETL and found that the ZnO film that was prepared with the 2-methoxyethanol solvent showed a high PCE of 10.39% and also a good reproducibility in terms of performance. ZnO/$MAPbI_3$ films prepared by 2-methoxyethanol demonstrate higher absorbance in the range of 400–600 nm, lower PL emission intensity, and larger grain sizes than their IPA and ethanol counterparts.

Chavan et al. (2022) had developed a new organic ligand-free organometallic approach to synthesize the ZnO quantum dots (QDs) for the ZnO ETL. The developed ZnO QDs were capped by easily removable dimethyl sulfoxide (DMSO) molecules. Furthermore, the developed QDs were spin-coated and needed only a 150 °C post-annealing treatment up to 10 min only for the growth of the ZnO ETL layer. The developed ZnO ETL showed better uniformity, better charge extraction, and better band alignment with perovskite than the ETL deposited by usual sol–gel-processed ZnO. The device based on these newly developed ZnO QDs resulted in a champion PCE of 20.05%. Leng et al. (2021) treated the ZnO nanoparticle-processed ETL via 4,7-dichloro-1,10-phenanthroline (Cl-phen) and 1,10-bathophenanthroline (BPhen). This can suppress the -OH group content on the ZnO surface. Furthermore, the Cl-phen modification reduced the energy gap between CBM OF ZnO and LUMO of perovskite from 0.29eV to 0.06eV, as shown in Figure 6. This enhanced the charge extraction and resulted in a champion PCE of 21.15%.

## 3.3 Tin(II) oxide ($SnO_2$)

Tin (II) oxide ($SnO_2$) is also an emerging material for ETL purposes and as a replacement of $TiO_2$ in PSCs. It has a large band gap of around 3.6 eV, higher bulk electron mobility (100–200 $cm^2V^{-1}sec^{-1}$), and high transparency to the visible light spectrum (~90%) (Sun et al., 2011; Wang et al., 2020a). In addition, the deposition and crystallization of the $SnO_2$ film can be carried out at a comparatively lower processing temperature (≤200 °C) than $TiO_2$. The performance of some $SnO_2$ ETL based PSCs have been summarized in Table 4. Song et al. (2015) had also reported that $SnO_2$ has better environmental stability than $TiO_2$. $SnO_2$ is widely used in the planar heterojunction PSCs as compared to the mesoscopic structure, i.e., the compact $SnO_2$ (c-$SnO_2$) has been investigated widely for ETL purposes. Ke et al. (2015) first investigated the solution-processed $SnO_2$ films in PSCs, which were deposited via spin coating of the precursor of $SnCl_2$ (dissolved in ethanol) with annealing at 180 °C, and the corresponding devices (i.e., FTO/$SnO_2$/$MAPbI_3$/spiro-OMeTAD/Au) gave the best PCE of 17.21% with small hysteresis, as shown in Figure 7.

Anaraki et al. (2016) had opted for the chemical bath deposition (CBD) method for the deposition of the $SnO_2$ ETL in mixed perovskite-based PSCs, which result in the best PCE of 20.8%. Liu et al. (2016) had used the dual combustion method for preparing the precursor of $SnO_2$. In this, $SnCl_2$ and ammonium nitrate ($NH_4NO_3$) were used as the combined oxidizer, while urea and acetylacetone as the fuel to the reaction. This method lowers the annealing temperature of $SnO_2$ to 140 °C, but the corresponding PSCs show severe hysteresis and the PCE remains only 12.93%, which further increases to 15.18% via passivation of $SnO_2$ with

**TABLE 4 Performance of $SnO_2$-based PSCs.**

| Deposition technique | Precursor | Device structure | Annealing temperature | $V_{oc}$ (%) | $J_{sc}$ (mA/cm$^2$) | F.F. | PCE (%) | Year | Reference |
|---|---|---|---|---|---|---|---|---|---|
| Spray pyrolysis | Butyl-(tin chloride) and $SnO_2$ nanoparticles | FTO/$SnO_2$/m-$SnO_2$/$MAPbI_3$/spiro-OMeTAD/Au | 500 °C | 0.93 | 17.38 | 0.62 | 10.18 | 2015 | Li et al. (2015) |
| Spin coating | $SnO_2$ nanoparticles in butanol | ITO/$SnO_2$/$MAPbI_3$/spiro-OMeTAD/Ag | 200 °C | 1.08 | 19.5 | 0.62 | 13.0 | 2015 | Song et al. (2015) |
| Spin coating | $SnCl_2{\cdot}2H_2O$ + Ethanol | FTO/$SnO_2$/$MAPbI_3$/spiro-OMeTAD/Au | 180 °C | 1.11 | 23.27 | 0.67 | 17.21 | 2015 | Ke et al. (2015) |
| Spin coating + CBD | $SnCl_2{\cdot}2H_2O$ | FTO/$SnO_2$/mixed perovskite/spiro-OMeTAD/Au | 180 °C | 1.17 | 22.59 | 0.75 | 20.8 | 2016 | Anaraki et al. (2016) |
| Spin coating | $SnCl_2$ + $NH_4NO_3$ + urea + acetyl acetone in 2-methoxyethanol | ITO/$SnO_2$/$MAPbI_3$/spiro-OMeTAD/Ag | 140 °C | 1.08 | 19.01 | 0.63 | 12.93 | 2016 | Liu et al. (2016) |
| Spin coating | Butyltin trichloride for $SnO_2$ and $SnCl_4{\cdot}5H_2O$ for m-$SnO_2$ | AZO/$SnO_2$/m-$SnO_2$/perovskite/spiro-OMeTAD/Au | 450 °C | 0.98 | 21.1 | 0.98 | 13.1 | 2016 | Roose et al. (2016) |
| Spin coating | $SnCl_2$ | FTO/$SnO_2$/$MAPbI_3$/CuSCN/Au | 200 °C | 0.96 | 18.99 | 0.45 | 8.38 | 2017 | Murugadoss et al. (2016) |
| Chemical bath deposition | $SnCl_4{\cdot}5H_2O$ in 2-propanol | FTO/$SnO_2$/mixed perovskite/SWNT + spiro-OMeTAD/Ag | 180 °C | 1.14 | 22.07 | 0.75 | 18.9 | 2017 | Habisreutinger et al. (2017) |
| Spin coating | $SnO_2$ nanoparticles | ITO/$SnO_2$/mixed perovskite/spiro-OMeTAD/Au | 150 °C | 1.12 | 23.86 | 0.80 | 21.64 | 2017 | Jiang et al. (2017) |
| Spin coating | $SnCl_2{\cdot}2H_2O$ | FTO/$SnO_2$/$CH_3NH_3PbI_{3-x}Cl_x$/Spiro-OMeTAD/Ag | 70 °C | 1.07 | 21.95 | 0.69 | 16.21 | 2017 | Huang et al. (2017b) |
| Chemical bath deposition | $SnCl_4{\cdot}5H_2O$ | ITO/$SnO_2$/$MAPbI_3$/Spiro-OMeTAD/Ag | 55 °C | 1.05 | 21.3 | 0.66 | 14.8 | 2017 | Barbé et al. (2017) |
| Spin coating | $SnCl_2{\cdot}2H_2O$ + Ethanol | FTO/$SnO_2$/$MAPbI_3$/carbon/Au | 180 °C | 1.03 | 19.50 | 0.64 | 14.20 | 2018 | Lin et al. (2018) |
| Spin coating | $SnCl_2{\cdot}2H_2O$+ $CN_2H_4S$ in water | FTO/$SnO_2$/mixed perovskite/spiro-OMeTAD/Au | 200 °C | 1.13 | 23.05 | 0.79 | 20.79 | 2018 | Yang et al. (2018) |
| Spin coating | $SnO_2$ colloidal solution | FTO/$SnO_2$/$MAPbI_3$/spiro-OMeTAD/Au | 150 °C | 1.08 | 20.4 | 0.76 | 19.4 | 2019 | Méndez et al. (2019) |
| Spin coating | $SnCl_2{\cdot}2H_2O$ | FTO/$SnO_2$/mixed perovskite/spiro-OMeTAD/Au | 50 °C | 1.16 | 22.4 | 0.78 | 20.5 | 2019 | Dong et al. (2019) |
| Spin coating | Colloidal $SnO_2$ + polyethylene glycol | FTO/m-$SnO_2$/mixed perovskite/spiro-OMeTAD/Au | 180 °C | 1.10 | 24.56 | 0.77 | 20.82 | 2020 | Wang et al. (2020a) |
| Spin coating | $SnO_2$ quantum dots | ITO/$SnO_2$/$MAPbI_3$/Spiro-OMeTAD/Ag | 200 °C | 1.08 | 21.85 | 0.74 | 17.66 | 2020 | Wang et al. (2020b) |
| Spin coating | $SnCl_2{\cdot}2H_2O$ and $SnO_2$ nanoparticles | ITO/a-$SnO_2$/c-$SnO_2$/mixed perovskite/Spiro-OMeTAD/Ag | 190 °C | 1.125 | 23.26 | 0.77 | 20.39 | 2020 | Lee et al. (2020) |
| Spin coating | Colloidal $SnO_2$ + $H_2O_2$ in water | ITO/$SnO_2$/mixed perovskite/spiro-OMeTAD/Au | 185 °C | 1.16 | 24.22 | 0.78 | 22.15 | 2021 | Wang et al. (2021) |
| Spin coating | $SnCl_2{\cdot}2H_2O$ in isopropanol | FTO/$SnO_2$/$Cs_{0.05}(FA_{0.83}MA_{0.17})_{0.95}(I_{0.83}Br_{0.17})_3$/Spiro-OMeTAD/Au | 200 °C | 1.17 | 23.3 | 0.71 | 19.5 | 2021 | Li et al. (2021) |
| Spin coating | $SnO_2$ QDs | FTO/$SnO_2$/$MAPbI_3$/Spiro-OMeTAD/Ag | - | 1.14 | 23.38 | 0.76 | 20.24 | 2021 | Xu et al. (2021) |
| Spin coating | Colloidal $SnO_2$ | ITO/$SnO_2$/$FAPbI_3$/Spiro-OMeTAD/MoO3/Ag | 150 °C | 1.14 | 25.24 | 0.81 | 23.31 | 2021 | Xiong et al. (2021) |

(Continued on following page)

**TABLE 4 (*Continued*) Performance of $SnO_2$-based PSCs.**

| Deposition technique | Precursor | Device structure | Annealing temperature | $V_{oc}$ (%) | $J_{sc}$ (mA/cm$^2$) | F.F. | PCE (%) | Year | Reference |
|---|---|---|---|---|---|---|---|---|---|
| Chemical bath deposition | $SnCl_2{\cdot}2H_2O$ | FTO/$SnO_2$/mixed perovskite/spiro-OMeTAD/Au | 170 °C | 1.18 | 25.14 | 0.84 | 25.2 | 2021 | Yoo et al. (2021) |
| Spin coating | Tin(IV) isopropoxide and $SnCl_4$ | FTO/$SnO_2$/$FAPbI_3$/spiro-OMeTAD/Au | 190 °C | 1.18 | 25.74 | 0.83 | 25.5 | 2021 | Min et al. (2021) |
| Spray deposition | Colloidal $SnO_2$ | FTO/$SnO_2$/mixed perovskite/spiro-OMeTAD/Au | 150 °C | 1.1 | 22.83 | 0.79 | 20.08 | 2022 | Kumar et al. (2022) |
| Spin coating | Colloidal $SnO_2$ | FTO/$SnO_2$/$MAPbI_3$/Spiro-OMeTAD/Ag | R.T. | 1.15 | 23.08 | 78.81 | 20.88 | 2022 | Xu et al. (2022) |
| Spin coating | Colloidal $SnO_2$ + $SnCl_2{\cdot}2H_2O$ + $NH_4Cl$ | FTO/$SnO_2$/$Cs_{0.05}(FA_{0.83}MA_{0.17})_{0.95}Pb(I_{0.83}Br_{0.17})_3$/Spiro-OMeTAD/Au | 120 °C | - | - | - | 21 | 2023 | Gil et al. (2023) |

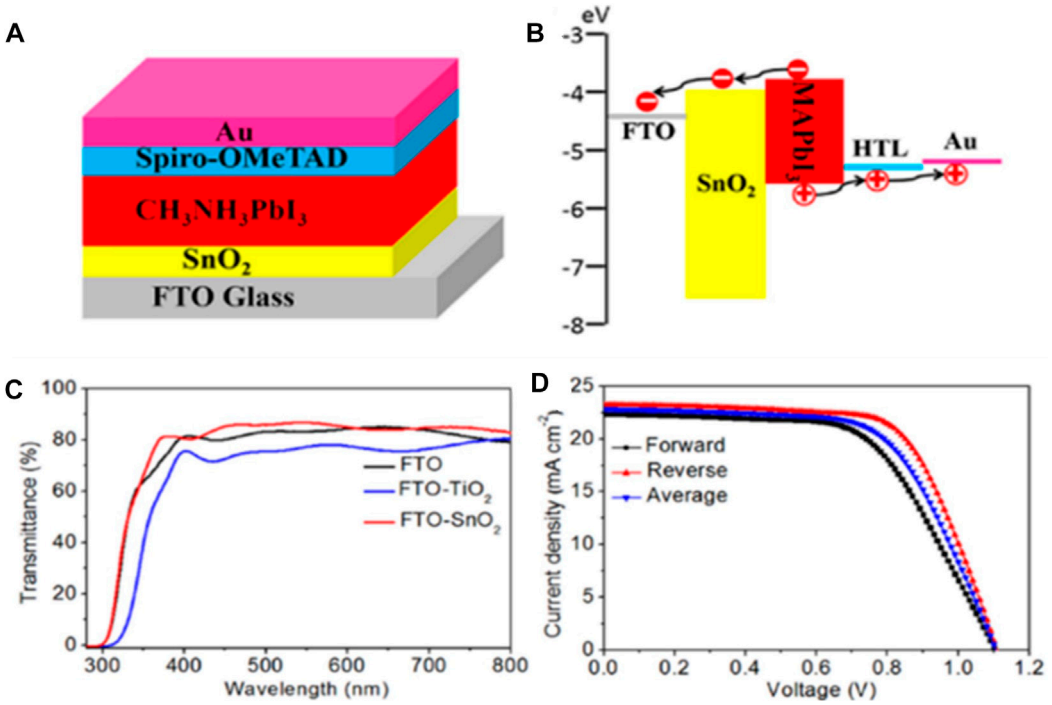


FIGURE 7
Schematic representation of **(A)** structure and **(B)** band diagram. FTO/$SnO_2$/$MAPbI_3$/spiro-OMeTAD/Au cells, **(C)** transmittance of FTO, $TiO_2$/FTO, and $SnO_2$/FTO, and **(D)** J-V curve of corresponding $SnO_2$ ETL-based PSCs. Reproduced with permission from Ke et al. (2015).

$C_{60}$-SAM (self-assembled monolayer). Jiang et al. (2017) had used the $SnO_2$ nanoparticles as the precursor solution and 150 °C annealing temperature for the $SnO_2$ ETL in mixed perovskite $((FAPbI_3)_{1-x}(MAPbBr_3)_x)$-based SCs, which resulted in the best PCE of 21.6% in the 0.0737 cm$^2$ area device and the 20.1% in 1 cm$^2$ area device. Huang et al. (2017b) investigated the low temperature (~70 °C) UV-sintered $SnO_2$ ETL in $CH_3NH_3PbI_{3-x}Cl_x$-based PSCs with the highest PCE of 16.21%. Barbé et al. (2017) had deposited the amorphous $SnO_2$ via CBD at only 55 °C without any further annealing for $MAPbI_3$-based PSCs, which result in the best PCE of 14.28%. Dong et al. (2019) had investigated the low-temperature (~50 °C)-processed and UV-treated $SnO_2$ ETL for mixed perovskite $[Cs_{0.05}(FA_{0.85}MA_{0.15})_{0.95}Pb(I_{0.85}Br_{0.15})_3]$-based PSCs. The PSCs yielded the best PCEs of 20.5% and 17.5% on rigid and flexible substrates, respectively. A bilayer $SnO_2$ of amorphous-crystalline hetero phase has been studied by Lee et al. (2020) in the triple cation perovskite-based PSCs, which yield a best PCE of 20.39% and 14.93% for smaller (~0.09 cm$^2$) and larger (3.55 cm$^2$) active device areas, respectively. Recently, Wang et al. (2021) had modified the precursor of $SnO_2$ with an addition of hydrogen peroxide ($H_2O_2$). In comparison to the unmodified precursor-based $SnO_2$ film, the resultant modified

precursor-based $SnO_2$ film exhibits less trap density, improved electrical conductivity, outstanding film fabrication repeatability, and better energy level alignment, leading to significantly higher charge carrier extraction. The corresponding PSCs yield a best and a stabilized PCE of 22.15% and 21.9%, respectively, having a reduced hysteresis effect as compared to the devices based on an un-modified $SnO_2$ precursor.

In addition to the compact layer $SnO_2$, mesoscopic $SnO_2$ (m-$SnO_2$)-based PSCs have also been reported. Li et al. (2015) first reported PSCs based on m-$SnO_2$ annealed at 450 °C, which resulted in a best PCE of 6.50% without any treatment of the $SnO_2$ surface and a PCE of 10.18% with surface treatment via $TiCl_4$. Roose et al. (2016) had investigated the m-$SnO_2$-based PSCs on FTO and AZO substrates having the structures FTO/$SnO_2$/m-$SnO_2$/perovskite/spiro-OMeTAD/Au and AZO/$SnO_2$/m-$SnO_2$/perovskite/spiro-OMeTAD/Au, respectively. For this, the compact $SnO_2$ has been synthesized via spray pyrolysis, while m-$SnO_2$ has been synthesized via spin coating of the precursor, followed by annealing at 450 °C. The PSCs on AZO substrates show better performance than those on FTO substrates with the best PCE of 13.1%. The aforementioned mesoscopic scaffold $SnO_2$ ETLs require a high temperature for growth, which hinders the growth of flexible PSCs. So a low-temperature (~180 °C) processable m-$SnO_2$-based PSCs have been reported by Wang et al. (2020a). To optimize the m-$SnO_2$ layer, polyethylene glycol has been introduced in the colloidal $SnO_2$ precursor and the PEG can be removed from the film through low-temperature annealing, which resulted in a mesoporous $SnO_2$ film. The corresponding mixed perovskite $[(Cs_{0.05}FA_{0.95}PbI_3)_{0.97}(MAPbBr_3)_{0.03}]$-based PSCs show a best PCE of 20.82%. Xiong et al. (2021) introduced polyethylene glycol diacrylate (PEGDA) in $SnO_2$ dispersion solution to avoid agglomeration in the $SnO_2$ film for ITO/$SnO_2$/$FAPbI_3$/Spiro-OMeTAD/$MoO_3$/Ag PSCs. The PEGDA-modified $SnO_2$ films were more uniform than the pristine $SnO_2$ films, and the energy level of the modified film matched well with the perovskite, which improves the carrier transfer and reduces the energy loss. This resulted in a higher $V_{oc}$ of 1.14 V and a high PCE of 23.31%. Yoo et al. (2021) had opted the CBD route for the $SnO_2$ ETL deposition in FTO/$SnO_2$/mixed perovskite/spiro-OMeTAD/Au PSCs. They studied the changes in $SnO_2$ film deposition with reaction time. During the $SnO_2$ film deposition, the decomposition pathway of the $SnO_2$ precursor (i.e., $SnCl_2$) depends on the pH of the solution, which changes with the reaction time as urea present in the precursor decomposes and releases $OH^-$. Initially, for pH ~1–1.5, the dominant product of deposition was $SnO_2$, and later on at pH = 3, the incomplete oxidation of $Sn^{2+}$ to $Sn^{4+}$ occurred due to the reduced amount of oxygen in the precursor solution, resulting in the $SnO_{2-x}$ phase. For higher pH~6, $(Sn_6O_4(OH)_4$ and SnO are produced, which are non-electron transporting phases. So, by optimizing the time of deposition, these phases can be avoided. The PSCs based on the ETL with $SnO_2$ and $SnO_{2-x}$ phases yielded a high PCE of up to 24.4% with a certified PCE of 25.2%. Min et al. (2021) had reported a certified champion PCE of 25.5%, introducing an interlayer between the $SnO_2$ ETL and $FAPbI_3$ perovskite layer. They used the $Cl^-$ ion-based precursor for the $SnO_2$ layer and also introduced the $Cl^-$ ions in $FAPbI_3$. This introduced an interlayer of $FASnCl_x$ between $SnO_2$ and $FAPbI_3$, which can enhance the charge extraction and reduce the recombination, leading to a high PCE.

## 3.4 Tungsten oxide ($WO_x$)

In PSCs, $WO_x$ has also been investigated by many research groups as an alternative to $TiO_2$. It shows a band gap of 2.6–3.1 eV varying according to its crystal structure (Berak and Sienko, 1970; Wang et al., 2012; Wang et al., 2017a). Although its band gap is smaller than $TiO_2$, it shows high stability, and it also has a high electron mobility (10–20 $cm^2 V^{-1} s^{-1}$) in comparison to $TiO_2$ (Wang et al., 2016). The performance of some $WO_x$ ETL based PSCs have been summarized in Table 5. Mahmood et al. (2015) had explored hydrothermally grown tungsten trioxide ($WO_3$)-based nanostructures like 0-D nanoparticles, 1-D nanorods, and 3-D nanosheet arrays to fabricate porous ETL by using the electrospray method. In these, the 2-D nanosheet-$WO_3$ film yielded enhanced carrier transport as compared to the nanorods or nanoparticles, which resulted in a PCE of 11.24% in FTO/$WO_3$-nanosheet/$TiO_2$/$MAPbI_3$/spiro-OMeTAD/Ag configuration devices. Wang et al. (2016) had prepared amorphous $WO_x$ at 150 °C as the ETL for PSCs by using the spin coating method. The pristine $WO_x$-based cell yielded a PCE of 10.42%, and with a composite of $WO_x$-$TiO_x$, the performance increased to a PCE of 14.47%. When the annealing temperature of $WO_x$-$TiO_x$ layer decreased to 70 °C, corresponding PSCs yielded a best PCE of 13.45%. Wang et al. (2017a) had investigated the low-temperature (120 °C) annealed film of $WO_x$ and Nb-doped $WO_x$, i.e., W(Nb)$O_x$ in the flexible PSCs. The cell with pristine $WO_x$ yielded a PCE of 14.59%, and the introduction of Nb had increased the PCE to 15.65%. Chen et al. (2020) had prepared a solution-processed nano-crystalline $WO_x$ film at ultra-low temperature (50 °C) by using the precursor of $WCl_6$ dissolved in different alcohols like ethanol, butanol, and hexanol named as E-$WO_x$, B-$WO_x$, and H-$WO_x$. The PSCs produced by using the hexanol solvent and mixed perovskite have resulted in the best performance with a higher PCE of 20.77%, less charge recombination sites, and higher carrier mobility than the film produced by using other solvents.

## 3.5 Indium oxide ($In_2O_3$)

Indium oxide ($In_2O_3$), having a wide band gap (~3.75 eV) and a high carrier mobility (~20 $cm^2 V^{-1} s^{-1}$), is also a promising alternative to $TiO_2$ (Korotcenkov et al., 2005), (Lau et al., 2015). It also shows high transparency and good thermal stability. The performance of some $In_2O_3$ ETL based PSCs have been summarized in Table 6. In 2016, Qin et al. (2016) optimized the precursor ($In(NO_3)_3 \cdot 4.5H_2O$+ ethanol) concentration and the annealing temperature (200 °C) of the solution-processed film of $In_2O_3$ for the $MAPbI_3$-based PSCs. The PSCs with only $In_2O_3$ as an ETL have exceeded a PCE of 13%, and when it was used in combination with PCBM as other ETL, the cell yielded a best PCE of 14.83%. Chen et al. (2017) had also used the spin coating method to prepare the film of $In_2O_3$ for the PSCs, but the precursor of [$In(NO_3)_3 \cdot 4.5H_2O$+ ethanol] has been modified by adding acetylacetone to chelate $In^{3+}$ and stabilize the precursor, which yielded the PCE of the cell (ITO/

**TABLE 5 Performance of $WO_x$-based PSCs.**

| Deposition technique | Precursor | Device structure | Annealing temperature | $V_{oc}$ (V) | $J_{sc}$ (mA/cm$^2$) | F.F. | PCE (%) | Year | Reference |
|---|---|---|---|---|---|---|---|---|---|
| Electro spray | $H_2WO_4$ | FTO/$WO_3$-nanosheet/$TiO_2$/$MAPbI_3$/spiro-OMeTAD/Ag | 500 °C | 0.870 | 17.0 | 0.76 | 11.24 | 2015 | Mahmood et al. (2015) |
| Spin coating | $WCl_6$ | FTO/$WO_x$/$CH_3NH_3PbI_xCl_{1-x}$/spiro-OMeTAD/Ag | 150 °C | 0.71 | 21.77 | 0.58 | 8.99 | 2015 | Wang et al. (2015) |
| Spin coating | $WO_x$ in iso-propanol | ITO/$WO_x$/perovskite/spiro-OMeTAD/Ag | 140 °C | 0.75 | 21.8 | 0.65 | 10.7 | 2015 | Hou et al. (2015) |
| Spin coating | $WO_x$ in iso-propanol | ITO/$WO_x$/$C_{60}$-SAM/perovskite/spiro-OMeTAD/Ag | 140 °C | 1.02 | 21.9 | 0.66 | 14.9 | 2015 | Hou et al. (2015) |
| Spin coating | $WCl_6$ | FTO/$WO_x$/$CH_3NH_3PbI_xCl_{1-x}$/spiro-OMeTAD/Ag | 150 °C | 0.81 | 18.91 | 0.68 | 10.42 | 2016 | Wang et al. (2016) |
| Spin coating | $WCl_6$ | FTO/$WO_x$-$TiO_x$/$CH_3NH_3PbI_xCl_{1-x}$/spiro-OMeTAD/Ag | 150 °C | 0.89 | 23.07 | 0.71 | 14.47 | 2016 | Wang et al. (2016) |
| Spin coating | Tungsten isopropoxide | FTO/$WO_x$/mixed perovskite/spiro-OMeTAD/Au | 500 °C | 0.77 | 18.12 | 0.73 | 10.14 | 2016 | Zhang et al. (2016) |
| Spin coating | $H_2WO_4$ | FTO/$WO_3$ nano-particles layer/$Cs_2CO_3$/PCBM/$MAPbI_3$/P3HT/Au | 450 °C | 0.84 | 20.40 | 0.61 | 10.49 | 2016 | Chen et al. (2016) |
| Spin coating | $W(OCH_2CH_3)_5$ | PEN/ITO/$WO_x$/perovskite/spiro-OMeTAD/Ag | 120 °C | 0.91 | 22.31 | 0.72 | 14.59 | 2017 | Wang et al. (2017a) |
| Spin coating | $W(OCH_2CH_3)_5$ and $Nb(OCH_2CH_3)_5$ | PEN/ITO/W(Nb)$O_x$/perovskite/spiro-OMeTAD/Ag | 120 °C | 0.98 | 21.41 | 0.75 | 15.65 | 2017 | Wang et al. (2017a) |
| Spin coating | $WCl_6$ | FTO/$WO_x$/$C_{60}$/$MAPbI_3$/spiro-OMeTAD/Au | 150 °C | 0.93 | 22.15 | 0.78 | 16.07 | 2017 | Eze et al. (2017) |
| Spin coating | $WO_{3-x}$ carved nanorods in $CHCl_3$ | ITO/$WO_{3-x}$/$MAPbI_3$/$PC_{60}BM$/LiF-Al | RT | 0.87 | 20.7 | 0.74 | 13.3 | 2018 | Masi et al. (2018) |
| Spin coating | $WCl_6$ | FTO/$WO_x$/mixed perovskite/spiro-OMeTAD/Ag | 50 °C | 1.06 | 24.82 | 0.79 | 20.77 | 2020 | Chen et al. (2020) |

**TABLE 6 Performance of $In_2O_3$-based PSCs.**

| Deposition technique | Precursor | Device structure | Annealing temperature | $V_{oc}$ (V) | $J_{sc}$ (mA/cm$^2$) | F.F. | PCE (%) | Year | Reference |
|---|---|---|---|---|---|---|---|---|---|
| Spin coating | $In(NO_3)_3 \cdot 4.5H_2O$ | FTO/$In_2O_3$/PCBM/$MAPbI_3$/Spiro-OMeTAD/Au | 200 °C | 1.08 | 20.06 | 0.68 | 14.83 | 2016 | Qin et al. (2016) |
| Spin coating | $In(NO_3)_3 \cdot 4.5H_2O$+ acetylacetone in ethanol | ITO/$In_2O_3$/$MAPbI_3$/Spiro-OMeTAD/Ag | 200 °C | 1.05 | 21.3 | 0.68 | 15.3 | 2017 | Chen et al. (2017) |
| Spin coating | $In(NO_3)_3 \cdot xH_2O$ | ITO/$In_2O_3$/$MAPbI_3$/PTAA/Au | 300 °C | 1.03 | 22.48 | 0.63 | 14.63 | 2017 | Yoon et al. (2017) |
| Spin coating | $In(NO_3)_3 \cdot xH_2O$ + $NH_3 \cdot H_2O$+ acetylacetone in 2-methoxyethanol | ITO/$In_2O_3$/PCBM/mixed perovskite/Spiro-OMeTAD/Ag | 200 °C | 1.06 | 23.40 | 0.73 | 18.12 | 2019 | Guo et al. (2019b) |
| Spin coating | $In(NO_3)_3 \cdot xH_2O$+ acetylacetone in ethanol | FTO/$In_2O_3$/$MAPbI_3$/Spiro-OMeTAD/Au | 150 °C | 1.07 | 19.26 | 0.67 | 13.97 | 2020 | Zhang et al. (2020) |
| Spin coating | $In_2O_3$ nanoparticles | ITO/$NiO_x$/perovskite/Sn:$In_2O_3$/$In_2O_3$/Ag | - | 1.10 | 23.22 | 0.80 | 20.65 | 2021 | Yang et al. (2021b) |
| Spin coating | $In(NO_3)_3 \cdot xH_2O$ | FTO/$SnO_2$/$In_2O_3$/mixed perovskite/Spiro-OMeTAD/Ag | 180 °C | 1.15 | 23.87 | 0.82 | 25.18 | 2022 | Tian et al. (2022) |

$In_2O_3$/$MAPbI_3$/Spiro-OMeTAD/Ag) to be 15.3%. This modified precursor film of $In_2O_3$ has strongly quenched the photoluminescence (PL) emission peak intensity of perovskite, which indicates the efficient extraction of the carriers (i.e., the electrons) from the perovskite material. Guo et al. (2019b) used the fuel combustion method to prepare the precursor for spin coating the film of $In_2O_3$, and these films resulted in an electron mobility of 0.65 $cm^2V^{-1}s^{-1}$, and after modification with PCBM, the device having a structure of ITO/$In_2O_3$/PCBM/mixed perovskite/Spiro-OMeTAD/Ag resulted in the best PCE of 18.12%. Yang et al. (2021b) had demonstrated a gradient potential structure for the ETL by using the bilayer of pristine $In_2O_3$ and Sn-doped $In_2O_3$. This bilayer provided a gradient potential to the charge carrier, which enhanced the charge separation, extraction, and suppressed the charge recombination. This, as a result, enhanced the $V_{oc}$ of the device (1.05 V for pristine $In_2O_3$ to 1.10 V for the bilayer), leading to a device efficiency of 20.65% in the ITO/$NiO_x$/perovskite/Sn: $In_2O_3$/$In_2O_3$/Ag structure.

## 3.6 Niobium oxide ($NbO_x$)

Having a wide optical band gap (~4.1-eV), high transmission, higher carrier mobility, and a suitable conduction band energy level, $Nb_2O_5$ has also been investigated as an ETL and hole-blocking layer in PSCs (Yokoyama et al., 2020). The performance of some $NbO_x$ ETL based PSCs have been summarized in Table 7. Kogo et al. (2015) had studied solution-processed $Nb_2O_5$ as the hole-blocking layer in mesoporous $Al_2O_3$-based PSCs. The cells show a $V_{OC}$ up to 1.13 V, but the average PCE remains at only 8.8%. In this study, niobium ethoxide was used as a precursor to spin coat the film of niobium oxide. Zhang et al. (2018) investigated the different precursors like $NbCl_5$ in ethanol and niobium ethoxide in isopropanol and in ethanol to prepare the amorphous $NbO_x$ film for PSCs, which was treated with UV-ozone without any further annealing. It has been found that it is too obstinate to remove many counter ions and solvent molecules like the chloride ion, which have a strong ionic interaction with $Nb^{5+}$ and the IPA molecule by UVO treatment only. These impurities show an impact on the electrical properties like conductivity, carrier mobility, and defect concentration of the film, which further reduce the photovoltaic performance of the device. Furthermore, the ethanol molecules have a shorter molecular length, and the $C_2H_5O^-$ anion has a weak interaction with the $Nb^{5+}$ ion. So, these can easily be escaped from the film by UV treatment only. This is why niobium ethoxide and ethanol are suitable precursors to prepare the film of amorphous $NbO_x$. The $NbO_x$ film annealed at 500 °C has also been investigated, and it showed that high-temperature post-treatment is not required to achieve the high efficiency. The UVO-treated amorphous $NbO_x$ ETL-based PSCs with a FTO/$NbO_x$/mixed perovskite/spiro-OMeTAD/Ag structure have shown the best PCE of 19.09%. Furthermore, the amorphous $NbO_x$ ETL-based PSCs showed resistance against UV light because of the large band gap (~4.0 eV) of $NbO_x$, thus leading

**TABLE 7 Performance of $NbO_x$-based PSCs.**

| Deposition technique | Precursor | Device structure | Annealing temperature | $V_{OC}$ (V) | $J_{sc}$ (mA/cm$^2$) | F.F. | PCE (%) | Year | Reference |
|---|---|---|---|---|---|---|---|---|---|
| Spin coating | Niobium ethoxide | FTO/$Nb_2O_5$/m-$Al_2O_3$/$CH_3NH_3PbI_{3-x}Cl_x$/spiro-OMeTAD/Au | 500 °C | 1.11 ± 0.02 | 11.7 ± 1.1 | 0.67 ± 0.05 | 8.8 ± 1.5 | 2015 | Kogo et al. (2015) |
| Spin coating | Niobium ethoxide | FTO/$NbO_x$/$Cs_{0.05}$[$(FAPbI_3)_{0.85}$ $(MAPbBr_3)_{0.15}]_{0.95}$/spiro-OMeTAD/Ag | R.T. | 1.12 | 22.42 | 0.76 | 19.09 | 2018 | Zhang et al. (2018) |
| Spin coating | Niobium ethoxide | FTO/$Nb_2O_5$/mixed perovskite/spiro-OMeTAD/Au | 550 °C | 1.02 | 23.9 | 0.73 | 18.2 | 2018 | Shen et al. (2018) |
| Spin coating | Niobium oxalate powder | FTO/$Nb_2O_5$/$CH_3NH_3PbI_{3-x}Cl_x$/Spiro-OMeTAD/Au | 200 °C | 1.02 | 22.82 | 0.74 | 17.17 | 2018 | Guo et al. (2018) |
| Spin coating | Niobium(V) chloride | FTO/$Nb_2O_5$/$CH_3NH_3PbI_{3-x}Cl_x$/Spiro-OMeTAD/Ag | 500 °C | 1.02 | 21.63 | 0.68 | 14.82 | 2018 | Gu et al. (2018) |
| Spin coating | $Nb_2O_5$ colloidal solution | FTO/$Nb_2O_5$/mixed perovskite/spiro-OMeTAD/Au | 150 °C | 1.19 | 21.63 | 0.78 | 20.22 | 2019 | Wang et al. (2019b) |
| Spin coating | Nanosheets of $Nb_2O_5$ in ethanol | ITO/$NiO_x$/$CsPbI_2Br$/$Nb_2O_5$/$PC_{61}BM$/BPhen/Ag | - | 1.06 | 14.13 | 0.78 | 11.74 | 2019 | Han et al. (2019) |
| Spin coating | $Nb(C_2H_5O)_5$ and $Zn(NO_3)_2{\cdot}6H_2O$ (for doping) + $NH_4NO_3$ + acetylacetone in 2-methoxyethanol | FTO/Zn:$Nb_2O_5$/$MAPbI_3$/spiro-OMeTAD/Ag | 200 °C | 1.12 | 22.55 | 0.70 | 17.70 | 2019 | Ye et al. (2020) |

to enhancement of the stability of these PSCs. Wang et al. (2019b) had used the colloidal $Nb_2O_5$ solution to prepare the spin-coated film of $Nb_2O_5$ at low temperature (150 °C) for PSCs having an FTO/$Nb_2O_5$/mixed perovskite/spiro-OMeTAD/Au structure. The device displayed good stability, and the highest PCE of 20.22% and also a higher $V_{OC}$ of 1.19 V.

## 3.7 Cerium oxide ($CeO_x$)

Cerium oxide ($CeO_x$) is a rare-earth oxide that has a wide band gap (~3.5 eV), high ionic conductivity, large dielectric constant, and high thermal and chemical stability (Wang et al., 2017b). The performance of some $CeO_x$ ETL based PSCs have been summarized in Table 8. In 2017, Wang et al. (2017b) investigated a low temperature (~150 °C) and sol–gel-processable $CeO_x$ films as an ETL in PSCs having an FTO/$CeO_x$/$MAPbI_3$/spiro-OMeTAD/Ag structure. These solar cells show a best PCE of 14.32% with better stability than the devices with $TiO_2$ as the ETL, and when in addition to $CeO_x$, a $PC_{61}BM$ layer was introduced in PSCs; the PCE was improved to 17.04%. The introduction of $PC_{61}BM$ has improved the charge extraction and the transmittance of the ETL and hence the device performance. The HOMO and LUMO energy levels of $CeO_x$ were found to be −7.5 and −4.0, respectively, by this group, which is suitable for electron extraction and transportation, as well as blocking of holes in PSCs.

Hu et al. (2018) had investigated $CeO_x$ as an ETL in the inverted structure (ITO/$NiO_x$/Perovskite/$CeO_x$/Ag) PSCs. They prepared the $CeO_x$ film via solution process with the cerium (III) acetylacetonate hydrate as a precursor, followed by low-temperature (100 °C) annealing, and the devices based on these showed the best PCE of 17.1%. In a nitrogen environment, the devices based on $CeO_x$ retained more than 90% of their performance after 200 h, which was greater than their PCBM-based counterparts, in which 80% was retained after 160 h. This is because the $CeO_x$ film resists the pinhole formation from the Ag electrode side, which isolates the perovskite film, and its degradation gets slow. Fang et al. (2018) had opted for a precursor of $CeO_x$ nanocrystals in chlorobenzene to fabricate high-quality nanocrystalline films of $CeO_x$, which showed highly compact, pin-hole-free morphology and comparatively higher conductivity (~$10^{-4}$ S $cm^{-1}$). This method has been used in fabricating the devices having the inverted device structure, i.e., FTO/NiMgLiO/$MAPbI_3$/$CeO_x$/Ag, which showed a best PCE of 16.65%. When a $PC_{61}BM$ layer has been introduced in addition to the $CeO_x$ film, the best cell PCE improved to 18.69%. Pang et al. (2020) had demonstrated the low-temperature (80 °C) and UV-$O_3$ treated $CeO_x$ film in flexible PSCs having a PEN/ITO/$CeO_x$/$MAPbI_3$/spiro-OMeTAD/Au structure, which resulted in the best PCE of 14.63%.

# 4 Conclusion and outlook

In summary, we have provided a focused review of the different solution-processable metal oxide-based ETLs for PSCs. In metal oxides, $TiO_2$ has largely been investigated as an ETL material, but the necessity of a high temperature for film growth and crystallization, which leads to superior performance of the corresponding PSCs, hampers the development of flexible photovoltaic devices. For these, other materials like ZnO and $SnO_2$ have been investigated by researchers as an alternative to

**TABLE 8 Performance of $CeO_x$-based PSCs.**

| Deposition technique | Precursor | Device structure | Annealing temperature | $V_{oc}$ (V) | $J_{sc}$ (mA/cm$^2$) | F.F. | PCE (%) | Year | Reference |
|---|---|---|---|---|---|---|---|---|---|
| Spin coating | Cerium (III) 2,4-pentanedionate hydrate | FTO/$CeO_x$/$MAPbI_3$/spiro-OMeTAD/Ag | 150 °C | 1.04 | 21.93 | 0.62 | 14.32 | 2017 | Wang et al. (2017b) |
| Spin coating | Cerium (III) 2,4-pentanedionate hydrate | FTO/$CeO_x$/$PC_{61}BM$/$MAPbI_3$/spiro-OMeTAD/Ag | 150 °C | 1.06 | 23.25 | 0.69 | 17.04 | 2017 | Wang et al. (2017b) |
| Spin coating | Cerium (III) acetylacetonate hydrate | ITO/$NiO_x$/Perovskite/$CeO_x$/Ag | 100 °C | 1.04 | 20.43 | 0.79 | 17.1 | 2018 | Hu et al. (2018) |
| Spin coating | $CeO_x$ nano-crystals in chlorobenzene | FTO/NiMgLiO/$MAPbI_3$/$CeO_x$/Ag | - | 1.11 | 20.99 | 0.71 | 16.65 | 2018 | Fang et al. (2018) |
| Spin coating | $CeO_x$ nano-crystals solution | FTO/NiMgLiO/$MAPbI_3$/$PC_{61}BM$/$CeO_x$/Ag | - | 1.11 | 21.82 | 0.76 | 18.69 | 2018 | Fang et al. (2018) |
| Spin coating | Cerium (III) 2,4-pentanedionate hydrate | FTO/Cu:$NiO_x$/$MAPbI_3$/$PC_{61}BM$/$CeO_x$/Ag | 100 °C | 1.06 | 21.52 | 0.76 | 17.35 | 2018 | Xing et al. (2018) |
| Spin coating | Cerium (III) acetylacetonate hydrate | ITO/$NiO_x$/$CsPbIBr_2$/$CeO_x$/Ag | 100 °C | 1.01 | 8.76 | 0.63 | 5.60 | 2019 | Yang et al. (2019) |
| Spin coating | $CeO_x$ colloidal solution | PEN/ITO/$CeO_x$/$MAPbI_3$/spiro-OMeTAD/Au | 80 °C | 0.99 | 19.42 | 0.76 | 14.63 | 2020 | Pang et al. (2020) |

$TiO_2$. ZnO-based PSCs show lower stability because of the degradation of the perovskite material due to the existence of the hydroxyl (-OH) group on the ZnO surface. In addition, $SnO_2$ has emerged as a suitable low-temperature-processable ETL that has excellent optoelectronic properties, and the $SnO_2$ ETL-based PSCs achieved a remarkable PCE of ~25.5%. In addition to these, other metal oxides such as $CeO_x$, $NbO_x$, $InO_x$, and $WO_x$ have also been investigated as a solution-processable ETL in PSCs. These have shown many favorable improvements relating to the efficiency and stability of the PSCs, but these have not been investigated largely by the photovoltaic research community. These can also emerge as the facile ETL for PSCs in the future when these will be investigated as ETLs in the PSCs largely, and more attention will be given to engineering the optoelectronic properties of these in favor of the emergence of excellent ETLs for PSCs.

## Author contributions

All authors listed have made a substantial, direct, and intellectual contribution to the work and approved it for publication.

## Acknowledgments

One of the authors HS, acknowledges UGC for grant of SRF. Authors are also very thankful to Dr. Venu Gopal Achanta, Director CSIR-NPL, INDIA for his constant encouragement and support to carry out these studies.

## Conflict of interest

The authors declare that the research was conducted in the absence of any commercial or financial relationships that could be construed as a potential conflict of interest.

## Publisher's note

All claims expressed in this article are solely those of the authors and do not necessarily represent those of their affiliated organizations, or those of the publisher, the editors, and the reviewers. Any product that may be evaluated in this article, or claim that may be made by its manufacturer, is not guaranteed or endorsed by the publisher.

## References

Aamir, M., Adhikari, T., Sher, M., Revaprasadu, N., Khalid, W., Akhtar, J., et al. (2018). Fabrication of planar heterojunction CsPbBr 2 I perovskite solar cells using ZnO as an electron transport layer and improved solar energy conversion efficiency. *New J. Chem.* 42 (17), 14104–14110. doi:10.1039/C8NJ02238K

Ahmadi, S. H., Ghaffarkani, M., Ameri, M., Safari, N., and Mohajerani, E. (2020). Solvent selection for fabrication of low temperature ZnO electron transport layer in perovskite solar cells. *Opt. Mater (Amst)* 106, 109977. doi:10.1016/j.optmat.2020.109977

Anaraki, E. H., Kermanpur, A., Steier, L., Domanski, K., Matsui, T., Tress, W., et al. (2016). Highly efficient and stable planar perovskite solar cells by solution-processed tin oxide. *Energy Environ. Sci.* 9 (10), 3128–3134. doi:10.1039/C6EE02390H

Andreani, L. C., Bozzola, A., Kowalczewski, P., Liscidini, M., and Redorici, L. (2019). Silicon solar cells: Toward the efficiency limits. *Adv. Phys. X* 4 (1), 1548305. doi:10.1080/23746149.2018.1548305

Ansari, M. I. H., Qurashi, A., and Nazeeruddin, M. K. (2018). Frontiers, opportunities, and challenges in perovskite solar cells: A critical review. *J. Photochem. Photobiol. C Photochem. Rev.* 35, 1–24. doi:10.1016/j.jphotochemrev.2017.11.002

Bao, Y., Wang, D., Hui, W., Gu, L., Chao, L., and Song, L. (2023). Honeycomb-type TiO $_2$ films toward a high tolerance to optical paths for perovskite solar cells. *ChemSusChem* 16 (2), e202201749. doi:10.1002/cssc.202201749

Barbé, J., Tietze, M. L., Neophytou, M., Murali, B., Alarousu, E., Labban, A. E., et al. (2017). Amorphous tin oxide as a low-temperature-processed electron-transport layer for organic and hybrid perovskite solar cells. *ACS Appl. Mater Interfaces* 9 (13), 11828–11836. doi:10.1021/acsami.6b13675

Bera, A., Wu, K., Sheikh, A., Alarousu, E., Mohammed, O. F., and Wu, T. (2014). Perovskite oxide SrTiO $_3$ as an efficient electron transporter for hybrid perovskite solar cells. *J. Phys. Chem. C* 118 (49), 28494–28501. doi:10.1021/jp509753p

Berak, J. M., and Sienko, M. J. (1970). Effect of oxygen-deficiency on electrical transport properties of tungsten trioxide crystals. *J. Solid State Chem.* 2 (1), 109–133. doi:10.1016/0022-4596(70)90040-X

Best Cell-Efficiency Chart (NREL) (2021). Best cell-efficiency Chart (NREL). Available at: https://www.nrel.gov/pv/cell-efficiency.html (accessed Feb. 01 2021).

Bi, D., Boschloo, G., Schwarzmüller, S., Yang, L., Johansson, E. M. J., and Hagfeldt, A. (2013). Efficient and stable CH3NH3PbI3-sensitized ZnO nanorod array solid-state solar cells. *Nanoscale* 5 (23), 11686. doi:10.1039/c3nr01542d

Brown, G. F., and Wu, J. (2009). Third generation photovoltaics. *Laser Phot. Rev.* 3 (4), 394–405. doi:10.1002/lpor.200810039

Chavan, R. D., Wolska-Pietkiewicz, M., Prochowicz, D., Jędrzejewska, M., Tavakoli, M. M., Yadav, P., et al. (2022). Organic ligand-free ZnO quantum dots for efficient and stable perovskite solar cells. *Adv. Funct. Mater* 32 (49), 2205909. doi:10.1002/adfm.202205909

Chen, C.-M., Lin, Z.-K., Huang, W.-J., and Yang, S.-H. (2016). WO3 nanoparticles or nanorods incorporating Cs2CO3/PCBM buffer bilayer as carriers transporting materials for perovskite solar cells. *Nanoscale Res. Lett.* 11 (1), 464. doi:10.1186/s11671-016-1670-8

Chen, C., Jiang, Y., Wu, Y., Guo, J., Kong, X., Wu, X., et al. (2020). Low-temperature-processed WO $_x$ as electron transfer layer for planar perovskite solar cells exceeding 20% efficiency. *Sol. RRL* 4 (4), 1900499. doi:10.1002/solr.201900499

Chen, P., Yin, X., Que, M., Liu, X., and Que, W. (2017). Low temperature solution processed indium oxide thin films with reliable photoelectrochemical stability for efficient and stable planar perovskite solar cells. *J. Mater Chem. A Mater* 5 (20), 9641–9648. doi:10.1039/C7TA00183E

Conings, B., Baeten, L., Jacobs, T., Dera, R., D'Haen, J., Manca, J., et al. (2014). An easy-to-fabricate low-temperature TiO 2 electron collection layer for high efficiency planar heterojunction perovskite solar cells. *Apl. Mater* 2 (8), 081505. doi:10.1063/1.4890245

Culu, A., Kaya, I. C., and Sonmezoglu, S. (2022). Spray-pyrolyzed tantalium-doped TiO $_2$ compact electron transport layer for UV-photostable planar perovskite solar cells exceeding 20% efficiency. *ACS Appl. Energy Mater* 5 (3), 3454–3462. doi:10.1021/acsaem.1c03848

Docampo, P., Ball, J. M., Darwich, M., Eperon, G. E., and Snaith, H. J. (2013). Efficient organometal trihalide perovskite planar-heterojunction solar cells on flexible polymer substrates. *Nat. Commun.* 4 (1), 2761. doi:10.1038/ncomms3761

Dong, Q., Li, J., Shi, Y., Chen, M., Ono, L. K., Zhou, K., et al. (2019). Improved SnO 2 electron transport layers solution-deposited at near room temperature for rigid or flexible perovskite solar cells with high efficiencies. *Adv. Energy Mater* 9, 1900834. doi:10.1002/aenm.201900834

Eze, V. O., Seike, Y., and Mori, T. (2017). Efficient planar perovskite solar cells using solution-processed amorphous WO x/fullerene C 60 as electron extraction layers. *Org. Electron* 46, 253–262. doi:10.1016/j.orgel.2017.04.024

Fang, R., Wu, S., Chen, W., Liu, Z., Zhang, S., Chen, R., et al. (2018). [6,6]-Phenyl-C $_{61}$ -butyric acid methyl ester/cerium oxide bilayer structure as efficient and stable electron transport layer for inverted perovskite solar cells. *ACS Nano* 12 (3), 2403–2414. doi:10.1021/acsnano.7b07754

GarcÃa-Sã¡nchez, M. F., Ortiz, A., Santana, G., Bizarro, M., Peña, J., Cruz-Gandarilla, F., et al. (2010). Synthesis and characterization of nanostructured cerium dioxide thin films deposited by ultrasonic spray pyrolysis. *J. Am. Ceram. Soc.* 93 (1), 155–160. doi:10.1111/j.1551-2916.2009.03374.x

Gheno, A., Thu Pham, T. T., Di Bin, C., Bouclé, J., Ratier, B., and Vedraine, S. (2017). Printable WO3 electron transporting layer for perovskite solar cells: Influence on device

performance and stability. *Sol. Energy Mater. Sol. Cells* 161, 347–354. doi:10.1016/j.solmat.2016.10.002

Gil, B., Yun, A. J., Lim, J., Cho, J., Kim, B., Ryu, S., et al. (2023). Design of SnO $_2$ electron transport layer in perovskite solar cells to achieve 2000 h stability under 1 sun illumination and 85 °C. *Adv. Mater Interfaces* 10 (11). doi:10.1002/admi.202202148

Green, M. A., Ho-Baillie, A., and Snaith, H. J. (2014). The emergence of perovskite solar cells. *Nat. Photonics* 8 (7), 506–514. doi:10.1038/nphoton.2014.134

Gu, B., Zhu, Y., Lu, H., Tian, W., and Li, L. (2018). Efficient planar perovskite solar cells based on low-cost spin-coated ultrathin Nb2O5 films. *Sol. Energy* 166, 187–194. doi:10.1016/j.solener.2018.03.054

Guo, H., Chen, H., Zhang, H., Huang, X., Yang, J., Wang, B., et al. (2019). Low-temperature processed yttrium-doped SrSnO3 perovskite electron transport layer for planar heterojunction perovskite solar cells with high efficiency. *Nano Energy* 59, 1–9. doi:10.1016/j.nanoen.2019.01.059

Guo, X., Lin, Z., Ma, J., Hu, Z., Su, J., Zhang, C., et al. (2019). Low temperature combustion synthesized indium oxide electron transport layer for high performance and stable perovskite solar cells. *J. Power Sources* 438, 226981. doi:10.1016/j.jpowsour.2019.226981

Guo, Y., Tao, J., Jiang, J., Zhang, J., Yang, J., Chen, S., et al. (2018). Low temperature solution deposited niobium oxide films as efficient electron transport layer for planar perovskite solar cell. *Sol. Energy Mater. Sol. Cells* 188, 66–72. doi:10.1016/j.solmat.2018.08.020

Habisreutinger, S. N., Wenger, B., Snaith, H. J., and Nicholas, R. J. (2017). Dopant-free planar n–i–p perovskite solar cells with steady-state efficiencies exceeding 18%. *ACS Energy Lett.* 2 (3), 622–628. doi:10.1021/acsenergylett.7b00028

Han, D., Xin, Y., Yuan, Q., Yang, Q., Wang, Y., Yang, Y., et al. (2019). Solution-processed 2D Nb 2 O 5 (001) nanosheets for inverted CsPbI 2 Br perovskite solar cells: Interfacial and diffusion engineering. *Sol. RRL* 3 (7), 1900091. doi:10.1002/solr.201900091

Han, W., Wang, Y., Wan, J., and Wang, D. (2022). Eliminating hysteresis of perovskite solar cells with hollow TiO2 mesoporous electron transport layer. *Chem. Res. Chin. Univ.* 38 (1), 117–122. doi:10.1007/s40242-022-1401-x

Hou, Y., Quiroz, C. O. R., Scheiner, S., Chen, W., Stubhan, T., Hirsch, A., et al. (2015). Low-temperature and hysteresis-free electron-transporting layers for efficient, regular, and planar structure perovskite solar cells. *Adv. Energy Mater* 5 (20), 1501056. doi:10.1002/aenm.201501056

Hu, T., Xiao, S., Yang, H., Chen, L., and Chen, Y. (2018). Cerium oxide as an efficient electron extraction layer for p–i–n structured perovskite solar cells. *Chem. Commun.* 54 (5), 471–474. doi:10.1039/C7CC08657A

Huang, A., Zhu, J., Zhou, Y., Yu, Y., Liu, Y., Yang, S., et al. (2017). One step spray-coated TiO 2 electron-transport layers for decent perovskite solar cells on large and flexible substrates. *Nanotechnology* 28 (1), 01LT02. doi:10.1088/0957-4484/28/1/01LT02

Huang, L., Sun, X., Li, C., Xu, J., Xu, R., Du, Y., et al. (2017). UV-sintered low-temperature solution-processed SnO 2 as robust electron transport layer for efficient planar heterojunction perovskite solar cells. *ACS Appl. Mater Interfaces* 9 (26), 21909–21920. doi:10.1021/acsami.7b04392

Hussain, I., Tran, H. P., Jaksik, J., Moore, J., Islam, N., and Uddin, M. J. (2018). Functional materials, device architecture, and flexibility of perovskite solar cell. *Emergent Mater* 1 (3–4), 133–154. doi:10.1007/s42247-018-0013-1

Im, J.-H., Jang, I.-H., Pellet, N., Grätzel, M., and Park, N.-G. (2014). Growth of CH3NH3PbI3 cuboids with controlled size for high-efficiency perovskite solar cells. *Nat. Nanotechnol.* 9 (11), 927–932. doi:10.1038/nnano.2014.181

Ito, S., Tanaka, S., Vahlman, H., Nishino, H., Manabe, K., and Lund, P. (2014). Carbon-Double-bond-free printed solar cells from TiO 2/CH 3 NH 3 PbI 3/CuSCN/Au: Structural control and photoaging effects. *ChemPhysChem* 15 (6), 1194–1200. doi:10.1002/cphc.201301047

Jarwal, D. K., Mishra, A. K., Baral, K., Kumar, A., Kumar, C., Rawat, G., et al. (2022). Performance optimization of ZnO nanorods ETL based hybrid perovskite solar cells with different seed layers. *IEEE Trans. Electron Devices* 69 (5), 2494–2499. doi:10.1109/TED.2022.3162552

Jeong, I., Park, Y. H., Bae, S., Park, M., Jeong, H., Lee, P., et al. (2017). Solution-processed ultrathin TiO 2 compact layer hybridized with mesoporous TiO 2 for high-performance perovskite solar cells. *ACS Appl. Mater Interfaces* 9 (42), 36865–36874. doi:10.1021/acsami.7b11901

Jiang, Q., Chu, Z., Wang, P., Yang, X., Liu, H., Wang, Y., et al. (2017). Planar-structure perovskite solar cells with efficiency beyond 21%. *Adv. Mater.* 29 (46), 1703852. doi:10.1002/adma.201703852

Jung, H. S., and Park, N.-G. (2015). Perovskite solar cells: From materials to devices. *Small* 11 (1), 10–25. doi:10.1002/smll.201402767

Ke, W., Fang, G., Liu, Q., Xiong, L., Qin, P., Tao, H., et al. (2015). Low-temperature solution-processed tin oxide as an alternative electron transporting layer for efficient perovskite solar cells. *J. Am. Chem. Soc.* 137 (21), 6730–6733. doi:10.1021/jacs.5b01994

Khambunkoed, N., Homnan, S., Gardchareon, A., Chattrapiban, N., Songsiriritthigul, P., Wongratanaphisan, D., et al. (2021). Fully-covered slot-die-coated ZnO thin films for reproducible carbon-based perovskite solar cells. *Mater Sci. Semicond. Process* 136, 106151. doi:10.1016/j.mssp.2021.106151

Khatibi, A., Razi Astaraei, F., and Ahmadi, M. H. (2019). Generation and combination of the solar cells: A current model review. *Energy Sci. Eng.* 7 (2), 305–322. doi:10.1002/ese3.292

Kim, H.-S., Lee, C. R., Im, J. H., Lee, K. B., Moehl, T., Marchioro, A., et al. (2012). Lead iodide perovskite sensitized all-solid-state submicron thin film mesoscopic solar cell with efficiency exceeding 9%. *Sci. Rep.* 2 (1), 591. doi:10.1038/srep00591

Kim, H.-S., Lee, J. W., Yantara, N., Boix, P. P., Kulkarni, S. A., Mhaisalkar, S., et al. (2013). High efficiency solid-state sensitized solar cell-based on submicrometer rutile TiO 2 nanorod and CH 3 NH 3 PbI 3 perovskite sensitizer. *Nano Lett.* 13 (6), 2412–2417. doi:10.1021/nl400286w

Kim, H.-S., Mora-Sero, I., Gonzalez-Pedro, V., Fabregat-Santiago, F., Juarez-Perez, E. J., Park, N. G., et al. (2013). Mechanism of carrier accumulation in perovskite thin-absorber solar cells. *Nat. Commun.* 4 (1), 2242. doi:10.1038/ncomms3242

Kim, H.-S., and Park, N.-G. (2014). Parameters affecting I – V hysteresis of CH 3 NH 3 PbI 3 perovskite solar cells: Effects of perovskite crystal size and mesoporous TiO 2 layer. *J. Phys. Chem. Lett.* 5 (17), 2927–2934. doi:10.1021/jz501392m

Kim, J., Kim, G., Kim, T. K., Kwon, S., Back, H., Lee, J., et al. (2014). Efficient planar-heterojunction perovskite solar cells achieved via interfacial modification of a sol–gel ZnO electron collection layer. *J. Mat. Chem. A* 2 (41), 17291–17296. doi:10.1039/C4TA03954H

Kogo, A., Numata, Y., Ikegami, M., and Miyasaka, T. (2015). Nb 2 O 5 blocking layer for high open-circuit voltage perovskite solar cells. *Chem. Lett.* 44 (6), 829–830. doi:10.1246/cl.150167

Kojima, A., Teshima, K., Shirai, Y., and Miyasaka, T. (2009). Organometal halide perovskites as visible-light sensitizers for photovoltaic cells. *J. Am. Chem. Soc.* 131 (17), 6050–6051. doi:10.1021/ja809598r

Korotcenkov, G., Brinzari, V., Ivanov, M., Cerneavschi, A., Rodriguez, J., Cirera, A., et al. (2005). Structural stability of indium oxide films deposited by spray pyrolysis during thermal annealing. *Thin Solid Films* 479 (1–2), 38–51. doi:10.1016/j.tsf.2004.11.107

Kumar, M. H., Yantara, N., Dharani, S., Graetzel, M., Mhaisalkar, S., Boix, P. P., et al. (2013). Flexible, low-temperature, solution processed ZnO-based perovskite solid state solar cells. *Chem. Commun.* 49 (94), 11089. doi:10.1039/c3cc46534a

Kumar, N., Lee, H. B., Sahani, R., Tyagi, B., Cho, S., Lee, J., et al. (2022). Room-temperature spray deposition of large-area SnO $_2$ electron transport layer for high performance, stable FAPbI $_3$ -based perovskite solar cells. *Small Methods* 6 (2), 2101127. doi:10.1002/smtd.202101127

Lau, L. N., Ibrahim, N. B., and Baqiah, H. (2015). Influence of precursor concentration on the structural, optical and electrical properties of indium oxide thin film prepared by a sol–gel method. *Appl. Surf. Sci.* 345, 355–359. doi:10.1016/j.apsusc.2015.03.129

Lee, H. B., Kumar, N., Ovhal, M. M., Kim, Y. J., Song, Y. M., and Kang, J. (2020). Dopant-free, amorphous–crystalline heterophase SnO 2 electron transport bilayer enables >20% efficiency in triple-cation perovskite solar cells. *Adv. Funct. Mater* 30 (24), 2001559. doi:10.1002/adfm.202001559

Lee, J.-W., Lee, T.-Y., Yoo, P. J., Grätzel, M., Mhaisalkar, S., and Park, N.-G. (2014). Rutile TiO2-based perovskite solar cells. *J. Mater Chem. A Mater* 2 (24), 9251. doi:10.1039/c4ta01786b

Lee, M. M., Teuscher, J., Miyasaka, T., Murakami, T. N., and Snaith, H. J. (2012). Efficient hybrid solar cells based on meso-superstructured organometal halide perovskites. *Science* 338 (6107), 643–647. doi:10.1126/science.1228604

Leng, S., Wang, L., Wang, X., Zhang, Z., Liang, J., Zheng, Y., et al. (2021). Bottom interfacial engineering for methylammonium-free regular-structure planar perovskite solar cells over 21%. *Sol. RRL* 5 (8), 2100285. doi:10.1002/solr.202100285

Li, F., Shen, Z., Weng, Y., Lou, Q., Chen, C., Shen, L., et al. (2020). Novel electron transport layer material for perovskite solar cells with over 22% efficiency and long-term stability. *Adv. Funct. Mater* 30 (45), 2004933. doi:10.1002/adfm.202004933

Li, T., Rui, Y., Wang, X., Shi, J., Wang, Y., Yang, J., et al. (2021). Grain size and interface modification via cesium carbonate post-treatment for efficient SnO $_2$ -based planar perovskite solar cells. *ACS Appl. Energy Mater* 4 (7), 7002–7011. doi:10.1021/acsaem.1c01055

Li, Y., Zhu, J., Huang, Y., Liu, F., Lv, M., Chen, S., et al. (2015). Mesoporous SnO 2 nanoparticle films as electron-transporting material in perovskite solar cells. *RSC Adv.* 5 (36), 28424–28429. doi:10.1039/C5RA01540E

Liang, C., Wu, Z., Li, P., Fan, J., Zhang, Y., and Shao, G. (2017). Chemical bath deposited rutile TiO 2 compact layer toward efficient planar heterojunction perovskite solar cells. *Appl. Surf. Sci.* 391, 337–344. doi:10.1016/j.apsusc.2016.06.171

Lin, S., Yang, B., Qiu, X., Yan, J., Shi, J., Yuan, Y., et al. (2018). Efficient and stable planar hole-transport-material-free perovskite solar cells using low temperature processed SnO2 as electron transport material. *Org. Electron* 53, 235–241. doi:10.1016/j.orgel.2017.12.002

Liu, B.-T., Guo, B.-W., and Balamurugan, R. (2020). Effect of polyethylene glycol incorporation in electron transport layer on photovoltaic properties of perovskite solar cells. *Nanomaterials* 10 (9), 1753. doi:10.3390/nano10091753

Liu, D., and Kelly, T. L. (2014). Perovskite solar cells with a planar heterojunction structure prepared using room-temperature solution processing techniques. *Nat. Photonics* 8 (2), 133–138. doi:10.1038/nphoton.2013.342

Liu, J., Yao, Y., Xiao, S., and Gu, X. (2018). Review of status developments of high-efficiency crystalline silicon solar cells. *J. Phys. D. Appl. Phys.* 51 (12), 123001. doi:10.1088/1361-6463/aaac6d

Liu, M., Johnston, M. B., and Snaith, H. J. (2013). Efficient planar heterojunction perovskite solar cells by vapour deposition. *Nature* 501 (7467), 395–398. doi:10.1038/nature12509

Liu, X., Tsai, K.-W., Zhu, Z., Sun, Y., Chueh, C.-C., and Jen, A. K.-Y. (2016). A low-temperature, solution processable tin oxide electron-transporting layer prepared by the dual-fuel combustion method for efficient perovskite solar cells. *Adv. Mater Interfaces* 3 (13), 1600122. doi:10.1002/admi.201600122

Lu, H., Zhong, J., Ji, C., Zhao, J., and Zhao, R. (2020). Fabricating an optimal rutile TiO2 electron transport layer by delicately tuning TiCl4 precursor solution for high performance perovskite solar cells. *Nano Energy* 68, 104336. doi:10.1016/j.nanoen.2019.104336

Mahmood, K., Swain, B. S., and Amassian, A. (2014). Double-layered ZnO nanostructures for efficient perovskite solar cells. *Nanoscale* 6 (24), 14674–14678. doi:10.1039/C4NR04383A

Mahmood, K., Swain, B. S., and Jung, H. S. (2014). Controlling the surface nanostructure of ZnO and Al-doped ZnO thin films using electrostatic spraying for their application in 12% efficient perovskite solar cells. *Nanoscale* 6 (15), 9127. doi:10.1039/C4NR02065K

Mahmood, K., Swain, B. S., Kirmani, A. R., and Amassian, A. (2015). Highly efficient perovskite solar cells based on a nanostructured WO 3 –TiO 2 core–shell electron transporting material. *J. Mater Chem. A Mater* 3 (17), 9051–9057. doi:10.1039/C4TA04883K

Mahmud, M. A., Elumalai, N. K., Upama, M. B., Wang, D., Chan, K. H., Wright, M., et al. (2017). Low temperature processed ZnO thin film as electron transport layer for efficient perovskite solar cells. *Sol. Energy Mater. Sol. Cells* 159, 251–264. doi:10.1016/j.solmat.2016.09.014

Mandati, S., Dileep, R. K., Veerappan, G., and Ramasamy, E. (2022). Large area bar coated TiO2 electron transport layers for perovskite solar cells with excellent performance homogeneity. *Sol. Energy* 240, 258–268. doi:10.1016/j.solener.2022.04.060

Masi, S., Mastria, R., Scarfiello, R., Carallo, S., Nobile, C., Gambino, S., et al. (2018). Room-temperature processed films of colloidal carved rod-shaped nanocrystals of reduced tungsten oxide as interlayers for perovskite solar cells. *Phys. Chem. Chem. Phys.* 20 (16), 11396–11404. doi:10.1039/C8CP00645H

Méndez, P. F., Muhammed, S. K. M., Barea, E. M., Masi, S., and Mora-Seró, I. (2019). Analysis of the UV–Ozone-Treated SnO 2 electron transporting layer in planar perovskite solar cells for high performance and reduced hysteresis. *Sol. RRL* 3 (9), 1900191. doi:10.1002/solr.201900191

Mesquita, I., Andrade, L., and Mendes, A. (2017). Perovskite solar cells: Materials, configurations and stability. *Renew. Sustain. Energy Rev.* 82, 2471–2489. doi:10.1016/j.rser.2017.09.011

Min, H., Lee, D. Y., Kim, J., Kim, G., Lee, K. S., Kim, J., et al. (2021). Perovskite solar cells with atomically coherent interlayers on SnO2 electrodes. *Nature* 598 (7881), 444–450. doi:10.1038/s41586-021-03964-8

Murugadoss, G., Kanda, H., Tanaka, S., Nishino, H., Ito, S., Imahori, H., et al. (2016). An efficient electron transport material of tin oxide for planar structure perovskite solar cells. *J. Power Sources* 307, 891–897. doi:10.1016/j.jpowsour.2016.01.044

Nguyen, M. H., Yoon, S.-H., and Kim, K.-S. (2022). Hydrothermally fabricated TiO2 heterostructure boosts efficiency of MAPbI3 perovskite solar cells. *J. Industrial Eng. Chem.* 106, 382–392. doi:10.1016/j.jiec.2021.11.013

Noh, Y. W., Jin, I. S., Park, S. H., and Jung, J. W. (2020). Room-temperature synthesis of ZrSnO4 nanoparticles for electron transport layer in efficient planar hetrojunction perovskite solar cells. *J. Mater Sci. Technol.* 42, 38–45. doi:10.1016/j.jmst.2019.11.008

Ono, L. K., Juarez-Perez, E. J., and Qi, Y. (2017). Progress on perovskite materials and solar cells with mixed cations and halide anions. *ACS Appl. Mater Interfaces* 9 (36), 30197–30246. doi:10.1021/acsami.7b06001

Orel, Z. C., and Orel, B. (1994). Optical properties of pure CeO2 and mixed CeO2/SnO2 thin film coatings. *Phys. status solidi (b)* 186 (1), K33–K36. doi:10.1002/pssb.2221860135

Pang, A., Li, J., Wei, X.-F., Ruan, Z.-W., Yang, M., and Chen, Z.-N. (2020). UV–O $_3$ treated annealing-free cerium oxide as electron transport layers in flexible planar perovskite solar cells. *Nanoscale Adv.* 2 (9), 4062–4069. doi:10.1039/D0NA00367K

Qin, M., Ma, J., Ke, W., Qin, P., Lei, H., Tao, H., et al. (2016). Perovskite solar cells based on low-temperature processed indium oxide electron selective layers. *ACS Appl. Mater Interfaces* 8 (13), 8460–8466. doi:10.1021/acsami.5b12849

Qin, P., Tanaka, S., Ito, S., Tetreault, N., Manabe, K., Nishino, H., et al. (2014). Inorganic hole conductor-based lead halide perovskite solar cells with 12.4% conversion efficiency. *Nat. Commun.* 5 (1), 3834. doi:10.1038/ncomms4834

Qiu, J., Qiu, Y., Yan, K., Zhong, M., Mu, C., Yan, H., et al. (2013). All-solid-state hybrid solar cells based on a new organometal halide perovskite sensitizer and one-dimensional TiO2 nanowire arrays. *Nanoscale* 5 (8), 3245. doi:10.1039/c3nr00218g

Ren, X., Wang, Z. S., and Choy, W. C. H. (2019). Device Physics of the carrier transporting layer in planar perovskite solar cells. *Adv. Opt. Mater* 7 (20), 1900407–1900423. doi:10.1002/adom.201900407

Rong, Y., Ku, Z., Mei, A., Liu, T., Xu, M., Ko, S., et al. (2014). Hole-Conductor-free mesoscopic TiO 2/CH 3 NH 3 PbI 3 heterojunction solar cells based on anatase nanosheets and carbon counter electrodes. *J. Phys. Chem. Lett.* 5 (12), 2160–2164. doi:10.1021/jz500833z

Roose, B., Baena, J. P. C., Gödel, K. C., Graetzel, M., Hagfeldt, A., Steiner, U., et al. (2016). Mesoporous SnO2 electron selective contact enables UV-stable perovskite solar cells. *Nano Energy* 30, 517–522. doi:10.1016/j.nanoen.2016.10.055

Seo, Y. S., Lee, C., Lee, K. H., and Yoon, K. B. (2005). 1:1 and 2:1 charge-transfer complexes between aromatic hydrocarbons and dry Titanium dioxide. *Angew. Chem. Int. Ed.* 44 (6), 910–913. doi:10.1002/anie.200461972

Shah, A. V., Platz, R., and Keppner, H. (1995). Thin-film silicon solar cells: A review and selected trends. *Sol. Energy Mater. Sol. Cells* 38 (1–4), 501–520. doi:10.1016/0927-0248(94)00241-X

Shen, D., Zhang, W., Li, Y., Abate, A., and Wei, M. (2018). Facile deposition of Nb 2 O 5 thin film as an electron-transporting layer for highly efficient perovskite solar cells. *ACS Appl. Nano Mater* 1 (8), 4101–4109. doi:10.1021/acsanm.8b00859

Shin, S. S., Yeom, E. J., Yang, W. S., Hur, S., Kim, M. G., Im, J., et al. (2017). Colloidally prepared La-doped BaSnO $_3$ electrodes for efficient, photostable perovskite solar cells. *Science* 356 (6334), 167–171. doi:10.1126/science.aam6620

Singh, T., Singh, J., and Miyasaka, T. (2016). Role of metal oxide electron-transport layer modification on the stability of high performing perovskite solar cells. *ChemSusChem* 9 (18), 2559–2566. doi:10.1002/cssc.201601004

Son, D.-Y., Im, J.-H., Kim, H.-S., and Park, N.-G. (2014). 11% efficient perovskite solar cell based on ZnO nanorods: An effective charge collection system. *J. Phys. Chem. C* 118 (30), 16567–16573. doi:10.1021/jp412407j

Song, J., Zheng, E., Bian, J., Wang, X. F., Tian, W., Sanhiera, Y., et al. (2015). Low-temperature SnO 2 -based electron selective contact for efficient and stable perovskite solar cells. *J. Mater Chem. A Mater* 3 (20), 10837–10844. doi:10.1039/C5TA01207D

Sun, Y., Seo, J. H., Takacs, C. J., Seifter, J., and Heeger, A. J. (2011). Inverted polymer solar cells integrated with a low-temperature-annealed sol-gel-derived ZnO film as an electron transport layer. *Adv. Mater.* 23 (14), 1679–1683. doi:10.1002/adma.201004301

Suzuki, T., Kosacki, I., Anderson, H. U., and Colomban, P. (2004). Electrical conductivity and lattice defects in nanocrystalline cerium oxide thin films. *J. Am. Ceram. Soc.* 84 (9), 2007–2014. doi:10.1111/j.1151-2916.2001.tb00950.x

Tian, W., Song, P., Zhao, Y., Shen, L., Liu, K., Zheng, L., et al. (2022). Monolithic bilayered in $_2$ O $_3$ as an efficient interfacial material for high-performance perovskite solar cells. *Interdiscip. Mater.* 1 (4), 526–536. doi:10.1002/idm2.12047

Tvrdy, K., and Kamat, P. V. (2011). Quantum dot solar cells. *Compr. Nanosci. Technol.* 1 (5), 257–275. doi:10.1016/B978-0-12-374396-1.00129-X

Wang, E., Chen, P., Yin, X., Wu, Y., and Que, W. (2020). Novel ethanol vapor annealing treatment of SnO2 quantum dots film for highly efficient planar heterojunction perovskite solar cells. *Org. Electron* 84, 105751. doi:10.1016/j.orgel.2020.105751

Wang, F., Di Valentin, C., and Pacchioni, G. (2012). Rational band gap engineering of WO3 photocatalyst for visible light water splitting. *ChemCatChem* 4 (4), 476–478. doi:10.1002/cctc.201100446

Wang, H., Liu, H., Ye, F., Chen, Z., Ma, J., Liang, J., et al. (2021). Hydrogen peroxide-modified SnO2 as electron transport layer for perovskite solar cells with efficiency exceeding 22%. *J. Power Sources* 481, 229160. doi:10.1016/j.jpowsour.2020.229160

Wang, K., Shi, Y., Dong, Q., Li, Y., Wang, S., Yu, X., et al. (2015). Low-temperature and solution-processed amorphous $WO_X$ as electron-selective layer for perovskite solar cells. *J. Phys. Chem. Lett.* 6 (5), 755–759. doi:10.1021/acs.jpclett.5b00010

Wang, K., Shi, Y., Gao, L., Chi, R., Shi, K., Guo, B., et al. (2017). W(Nb)O x -based efficient flexible perovskite solar cells: From material optimization to working principle. *Nano Energy* 31, 424–431. doi:10.1016/j.nanoen.2016.11.054

Wang, K., Shi, Y., Li, B., Zhao, L., Wang, W., Wang, X., et al. (2016). Amorphous inorganic electron-selective layers for efficient perovskite solar cells: Feasible strategy towards room-temperature fabrication. *Adv. Mater.* 28 (9), 1891–1897. doi:10.1002/adma.201505241

Wang, Q., Peng, C., Du, L., Li, H., Zhang, W., Xie, J., et al. (2020). Enhanced performance of perovskite solar cells via low-temperature-processed mesoporous SnO $_2$. *Adv. Mater Interfaces* 7 (4), 1901866. doi:10.1002/admi.201901866

Wang, R., Mujahid, M., Duan, Y., Wang, Z. K., Xue, J., and Yang, Y. (2019). A review of perovskites solar cell stability. *Adv. Funct. Mater* 29 (47), 1808843. doi:10.1002/adfm.201808843

Wang, X., Deng, L. L., Wang, L. Y., Dai, S. M., Xing, Z., Zhan, X. X., et al. (2017). Cerium oxide standing out as an electron transport layer for efficient and stable perovskite solar cells processed at low temperature. *J. Mater Chem. A Mater* 5 (4), 1706–1712. doi:10.1039/C6TA07541J

Wang, Z., Lou, J., Zheng, X., Zhang, W.-H., and Qin, Y. (2019). Solution processed Nb $_2$ O $_5$ electrodes for high efficient ultraviolet light stable planar perovskite solar cells. *ACS Sustain Chem. Eng.* 7 (7), 7421–7429. doi:10.1021/acssuschemeng.9b00991

Wojciechowski, K., Saliba, M., Leijtens, T., Abate, A., and Snaith, H. J. (2014). Sub-150 °C processed meso-superstructured perovskite solar cells with enhanced efficiency. *Energy Environ. Sci.* 7 (3), 1142–1147. doi:10.1039/C3EE43707H

Wu, Y., Yang, X., Chen, H., Zhang, K., Qin, C., Liu, J., et al. (2014). Highly compact TiO 2 layer for efficient hole-blocking in perovskite solar cells. *Appl. Phys. Express* 7 (5), 052301. doi:10.7567/APEX.7.052301

Xing, Z., Li, S. H., Wu, B. S., Wang, X., Wang, L. Y., Wang, T., et al. (2018). Photovoltaic performance and stability of fullerene/cerium oxide double electron transport layer superior to single one in p-i-n perovskite solar cells. *J. Power Sources* 389, 13–19. doi:10.1016/j.jpowsour.2018.03.079

Xiong, Z., Lan, L., Wang, Y., Lu, C., Qin, S., Chen, S., et al. (2021). Multifunctional polymer framework modified $SnO_2$ enabling a photostable α-$FAPbI_3$ perovskite solar cell with efficiency exceeding 23. *ACS Energy Lett.* 6 (11), 3824–3830. doi:10.1021/acsenergylett.1c01763

Xu, Z., Huang, L., Jiang, Y., Li, Z., Chen, C., He, Z., et al. (2022). Thermal annealing-free $SnO_2$ for fully room-temperature-processed perovskite solar cells. *ACS Appl. Mater Interfaces* 14 (36), 41037–41044. doi:10.1021/acsami.2c11488

Xu, Z., Jiang, Y., Li, Z., Chen, C., Kong, X., Chen, Y., et al. (2021). Rapid microwave-assisted synthesis of $SnO_2$ quantum dots for efficient planar perovskite solar cells. *ACS Appl. Energy Mater* 4 (2), 1887–1893. doi:10.1021/acsaem.0c02992

Yang, B., Ma, R., Wang, Z., Ouyang, D., Huang, Z., Lu, J., et al. (2021). Efficient gradient potential top electron transport structures achieved by combining an oxide family for inverted perovskite solar cells with high efficiency and stability. *ACS Appl. Mater Interfaces* 13 (23), 27179–27187. doi:10.1021/acsami.1c05284

Yang, G., Chen, C., Yao, F., Chen, Z., Zhang, Q., Zheng, X., et al. (2018). Effective carrier-concentration tuning of SnO 2 quantum dot electron-selective layers for high-performance planar perovskite solar cells. *Adv. Mater.* 30 (14), 1706023. doi:10.1002/adma.201706023

Yang, J., Siempelkamp, B. D., Mosconi, E., De Angelis, F., and Kelly, T. L. (2015). Origin of the thermal instability in $CH_3NH_3PbI_3$ thin films deposited on ZnO. *Chem. Mater.* 27 (12), 4229–4236. doi:10.1021/acs.chemmater.5b01598

Yang, J., Zhang, Q., Xu, J., Liu, H., Qin, R., Zhai, H., et al. (2019). All-inorganic perovskite solar cells based on CsPbIBr2 and metal oxide transport layers with improved stability. *Nanomaterials* 9 (12), 1666. doi:10.3390/nano9121666

Yang, Z., Chen, W., Mei, A., Li, Q., and Liu, Y. (2021). Flexible MAPbI3 perovskite solar cells with the high efficiency of 16.11% by low-temperature synthesis of compact anatase TiO2 film. *J. Alloys Compd.* 854, 155488. doi:10.1016/j.jallcom.2020.155488

Ye, X., Ling, H., Zhang, R., Wen, Z., Hu, S., Akasaka, T., et al. (2020). Low-temperature solution-combustion-processed Zn-Doped Nb2O5 as an electron transport layer for efficient and stable perovskite solar cells. *J. Power Sources* 448, 227419. doi:10.1016/j.jpowsour.2019.227419

Yella, A., Heiniger, L.-P., Gao, P., Nazeeruddin, M. K., and Grätzel, M. (2014). Nanocrystalline rutile electron extraction layer enables low-temperature solution processed perovskite photovoltaics with 13.7% efficiency. *Nano Lett.* 14 (5), 2591–2596. doi:10.1021/nl500399m

Yokoyama, T., Nishitani, Y., Miyamoto, Y., Kusumoto, S., Uchida, R., Matsui, T., et al. (2020). Improving the open-circuit voltage of Sn-based perovskite solar cells by band alignment at the electron transport layer/perovskite layer interface. *ACS Appl. Mater Interfaces* 12 (24), 27131–27139. doi:10.1021/acsami.0c04676

Yoo, J. J., Seo, G., Chua, M. R., Park, T. G., Lu, Y., Rotermund, F., et al. (2021). Efficient perovskite solar cells via improved carrier management. *Nature* 590 (7847), 587–593. doi:10.1038/s41586-021-03285-w

Yoon, S., Kim, S. J., Kim, H. S., Park, J. S., Han, I. K., Jung, J. W., et al. (2017). Solution-processed indium oxide electron transporting layers for high-performance and photo-stable perovskite and organic solar cells. *Nanoscale* 9 (42), 16305–16312. doi:10.1039/C7NR05695H

Zhang, C., Shi, Y., Wang, S., Dong, Q., Feng, Y., Wang, L., et al. (2018). Room-temperature solution-processed amorphous NbO x as an electron transport layer in high-efficiency photovoltaics. *J. Mater Chem. A Mater* 6 (37), 17882–17888. doi:10.1039/C8TA06436A

Zhang, J., Shi, C., Chen, J., Wang, Y., and Li, M. (2016). Preparation of ultra-thin and high-quality WO3 compact layers and comparision of WO3 and TiO2 compact layer thickness in planar perovskite solar cells. *J. Solid State Chem.* 238, 223–228. doi:10.1016/j.jssc.2016.03.033

Zhang, X., Li, J., Bi, Z., He, K., Xu, X., Xiao, X., et al. (2020). Stable and efficient air-processed perovskite solar cells employing low-temperature processed compact In2O3 thin films as electron transport materials. *J. Alloys Compd.* 836, 155460. doi:10.1016/j.jallcom.2020.155460

Zhou, Y., Li, X., and Lin, H. (2020). To Be higher and stronger—metal oxide electron transport materials for perovskite solar cells. *Small* 16 (15), 1902579. doi:10.1002/smll.201902579

Zhu, G., Shen, Y., Xu, K., Huangfu, M., Cao, M., Gu, F., et al. (2016). Preparation of ZnO electron transport layers by spray technology for perovskite solar cells. *J. Alloys Compd.* 689, 192–198. doi:10.1016/j.jallcom.2016.07.182

Zhu, M., Liu, W., Ke, W., Xie, L., Dong, P., and Hao, F. (2019). Graphene-modified tin dioxide for efficient planar perovskite solar cells with enhanced electron extraction and reduced hysteresis. *ACS Appl. Mater Interfaces* 11 (1), 666–673. doi:10.1021/acsami.8b15665